eLife – Research Article
23rd October 2025

Retrosplenial cortex enables context-dependent goal-directed sensorimotor transformation

Pol Bech[1,#,*], Robin F. Dard[1,#,*], Jules Lebert[1], Lana Smith[1], Axel Bisi[1], Anthony Renard[1], Sylvain Crochet[1,#,†], and Carl C.H. Petersen[1,#,†]

[1] Laboratory of Sensory Processing, Brain Mind Institute, School of Life Sciences, Ecole Polytechnique Fédérale de Lausanne (EPFL), CH-1015 Lausanne, Switzerland

*,† These authors contributed equally.

Correspondence:

Pol Bech	pol.bechvilaseca@epfl.ch
Robin Dard	robin.dard@epfl.ch
Sylvain Crochet	sylvain.crochet@epfl.ch
Carl Petersen	carl.petersen@epfl.ch

Summary

The ability to dynamically adjust a behavioral response to a stimulus depending on context is of critical importance for animals. To investigate the neural basis supporting context-dependent sensory processing we developed a behavioral task in which mice changed their response to a single whisker deflection according to a continuously present contextual cue. Through unbiased optogenetic inactivation mapping, we found that neuronal activity in sensory and motor cortices contributed to task execution and, interestingly, we uncovered an unexpected role of retrosplenial cortex for contextual integration. Widefield calcium imaging revealed that retrosplenial cortex was the first cortical area to show context discrimination in response to the whisker stimulus, followed by whisker motor cortex. Finally, we combined optogenetic inactivation with calcium imaging to define causal context-dependent changes in sensorimotor processing. Our cortex-wide mapping experiments thus begin to define key cortical nodes for context-dependent sensorimotor transformation and highlight an important contribution of retrosplenial cortex.

Introduction

In order to choose the appropriate action in response to a given sensory stimulus, animals typically need to integrate surrounding “contextual” information. While we begin to understand mechanisms underlying early sensory processing and the transformation of sensations into learned actions (Chen et al., 2024, 2015, 2017; Curtis and Kleinfeld, 2009; Esmaeili et al., 2021; Guo et al., 2014; Harris and Mrsic-Flogel, 2013; International Brain Laboratory et al., 2025; Khilkevich et al., 2024; Kim et al., 2021; Kleinfeld and Deschênes, 2011; Kwon et al., 2016; Mayrhofer et al., 2019; O’Connor et al., 2010; Resulaj et al., 2018; Sachidhanandam et al., 2013; Siegle et al., 2021; Yang et al., 2016), less is known regarding how functionally coupled sensorimotor associations can be dynamically modified by context (Allen et al., 2019; Banerjee et al., 2020; Chang et al., 2024; Chevée et al., 2022; Cole et al., 2024; Condylis et al., 2020; Gershman, 2017; Gilbert and Li, 2013; Kuchibhotla et al., 2017; Ortiz et al., 2020; Rossi-Pool et al., 2021; Wu et al., 2020).

The definition of context is large enough for multiple general categories to emerge. At its most fundamental level, people have often considered as context internal processes or states like motivation level, attention level or ongoing action. Decades of studies in this context modality have identified thalamocortical and neuromodulator-dependent disinhibitory mechanisms responsible for modifying sensory processing and cortical-network states (Crochet and Petersen, 2006; Eggermann et al., 2014; Gasselin et al., 2021; Lohani et al., 2022; Poort et al., 2022; Poulet et al., 2012; Poulet and Petersen, 2008; Saalmann et al., 2012; Urbain et al., 2015; Zhou et al., 2016). A different variation on context, this time considering the influence of external environmental stimuli on perception, learning, and memory, has been extensively studied in contextual fear/appetitive conditioning, navigation/foraging tasks, or working memory tasks. A large body of evidence in contextual fear conditioning shows it relies on well described circuits involving among others, the amygdala, the prelimbic system, the prefrontal cortex and the hippocampus (Tovote et al., 2015). Context-dependent navigation tasks depend on the ability of the hippocampus and associated regions such as the entorhinal cortex or the retrosplenial cortex to represent both spatial and context information. Interactions between the hippocampus and the prefrontal cortex supports context-dependent decision making in an exploration task (Place et al., 2016). Other studies have investigated the mechanisms underlying behavioral flexibility in rule changing paradigms in which context must be inferred by the animal. This ability to infer context and adjust a behavioral response accordingly depends on PFC (Birrell and Brown, 2000; Marton et al., 2018), orbitofrontal cortex (Banerjee et al., 2020; Klein-Flügge et al., 2022; Schoenbaum et al., 2009), premotor regions such as wM2 and ALM (Chang et al., 2024; Finkel et al., 2024), and anterior cingulate cortex (Cole et al., 2024; Hajnal et al., 2024). It is also possible to deconstruct context into a discrete sensory cue, like a pure tone or visual flash, to provide contextual information which modifies the contingency of a second upcoming stimulus. The ability to execute this type of tasks requires the maintenance of the information given by the first, context-setting cue to guide the response to the second cue, which is mediated by working memory. Many studies have shown that working memory is supported by prefrontal and medial prefrontal cortex (Asaad et al., 1998; Goldman-Rakic, 1995; Hasselmo, 2006; Liu et al., 2014; Romo et al., 1999; Stern et al., 2001). In mice, planification of movement execution relies on the anterolateral motor cortex (ALM), as well as wM2 (Esmaeili et al., 2021; Guo et al.,

2014). Recent work has presented evidence that ALM also contributes to context-dependent decisions in a delayed match to sample task (Wu et al., 2020), presumably by disrupting the working memory representations necessary for maintenance of the identity of the sample.

Multiple parallel streams of research have therefore investigated various important brain regions mediating context-dependent behaviors, with experiments conducted in mice increasingly aiming to probe causal circuit mechanisms through applying new advanced methodologies. Whether some of these mechanisms are shared across modalities of context-dependent behaviors remains to be investigated. Mice have a highly-developed array of facial whiskers, which they use to determine the size, shape, location and texture of objects in their immediate environment (Diamond et al., 2008; Feldmeyer et al., 2013; Petersen, 2019; Staiger and Petersen, 2021). Detection of a whisker deflection reported by licking for reward is among the simpler tasks explored to date, but nonetheless evidence suggests that many brain regions contribute to task execution, including various cortical regions, thalamus, striatum, and superior colliculus (El-Boustani et al., 2020; Kwon et al., 2016; Le Merre et al., 2018; Mayrhofer et al., 2019; Miyashita and Feldman, 2013; Oryshchuk et al., 2024; Sachidhanandam et al., 2013; Sippy et al., 2015; Takahashi et al., 2020; Yamashita and Petersen, 2016; Yang et al., 2016). Building on this relatively simple whisker detection task, we now begin to ask if we can adapt it to study specific circuits for contextual modulation of sensory processing. To address this question, here, we developed a context-dependent detection task where the reward contingency of a well-defined single-whisker sensory stimulus was modulated according to the texture of auditory background noise. Combining unbiased cortex-wide inactivation screening with widefield calcium imaging, we identified cortical regions involved in task execution and found that retrosplenial cortex appears to play a key role for integration of sensory stimuli and context.

Results

Rapid behavioral adaptation to sensory stimuli in a changing context

We trained head-fixed, water-restricted mice to adapt their response to a whisker sensory stimulus according to an explicitly and continuously given contextual cue in

the form of two distinct auditory background sounds (pink noise or brown noise). We deterministically alternated between contexts in blocks of 20 pseudo-randomly organized trials during single sessions. According to this changing context, mice were rewarded (or not) for licking a water spout within a 1-s response window following a brief (3 ms) stimulus of the C2 whisker, whereas licking after a brief (10 ms) auditory 10 kHz tone was always rewarded (Figure 1A). Thus, mice had to learn to lick for reward in response to the whisker stimulus only in the whisker-rewarded context (W+) and refrain from licking in the whisker-non-rewarded context (W-), while maintaining constant licking in response to the auditory pure tone in both contexts. In addition, no-stimulus trials (Catch) were randomly delivered to assess the spontaneous lick rate. Error licks in Catch trials or whisker stimulus trials in W- blocks were neither rewarded nor punished.

Mice were trained in this task until they reached expert performance, completing an average of 23 blocks per session (Figure 1B and Figure 1 – figure supplement 1A-D). In expert sessions, mice showed consistent licking responses to the auditory stimulus in both contexts (Auditory hit rate: W+ = 96 ± 4 %, W- = 94 ± 5 %; n = 41 mice), and strong context-modulated licking in response to whisker stimuli (W+ = 84 ± 6 %, W- = 32 ± 7 %) (Figure 1C), irrespective of which background noise was associated to each context (Figure 1D). Lick rates in catch trials were overall low, although slightly higher in W+ blocks (Catch false alarm rate: W+ = 13 ± 7 %, W-: 4 ± 2%; t-value = -9, p-value = 1.6×10^{-10}). The consistent lick responses to the auditory pure tone suggest that the modulation of the responses to the whisker stimulus is not due to disengagement. To test if mice used the background contextual information to guide their choices, we compared performance of a subset of mice in the original task (Context On) with a variation in which both context sounds were replaced by continuous white noise while preserving the underlying block reward structure (Context Off). After removing the explicit contextual information mice were unable to discriminate between context blocks (Figure 1E and Figure 1 – figure supplement 1E).

We next investigated how quickly mice adapted their responses to the whisker stimulus following context transition. Mice changed their licking behavior as early as the first whisker trial following the context transition with a slight gradual further adaptation over subsequent whisker trials (Figure 1F). The probability of licking in response to whisker deflection was significantly different comparing the first trial after

159 context change with the last trial of the previous block (transition from W- to W+: pre =
160 26 ± 8 %, post = 73 ± 13 %, t-value = 21, p-value = 2.8 x 10^{-23}; transition from W+ to
161 W-: pre = 87 ± 7 %, post = 57 ± 13 %, t-value = -14, p-value = 7.3 x 10^{-17}) (Figure 1G).
162 Since trials within each context block were pseudo-randomly ordered, the first whisker
163 trial could occur at variable delays after the context transition. To assess whether this
164 delay influenced the mouse response, we analyzed the lick probability to the first
165 whisker trial in either the W+ or W− context as a function of time elapsed since the
166 transition (Figure 1H). We observed a progressive increase in lick probability in W+
167 and a corresponding decrease in W−, suggesting temporal integration of contextual
168 information after context switch. However, there was no apparent sign of anticipation
169 of the context switch in the behavior of the mice.

170 Context could influence the mouse posture or uninstructed movements, which
171 could reflect active sensing or attentional changes (Musall et al., 2019). To investigate
172 context- or performance-specific behavioral changes in expert sessions, we performed
173 high-speed videography of the mouse face. Using pose estimation (Mathis et al.,
174 2018), we extracted dorsal and lateral orofacial kinematic features, including whisker
175 angle, jaw opening, and pupil area (Figures 1I&J and Figure 1 – figure supplement 1F-
176 H). We first sought to investigate whether the pre-stimulus baseline orofacial posture
177 and motion could reflect the current context and / or could predict a licking response
178 to the upcoming whisker stimulus. We analyzed the 2-s no-lick window before trial
179 onsets and computed the average position and speed. Our analysis revealed no
180 significant general effect of context for the average whisker angle or jaw opening, but
181 pupil area was larger in the W+ context, perhaps reflecting attentional state (McGinley
182 et al., 2015; Reimer et al., 2014) (Figure 1I and Figure 1 – figure supplement 1G).
183 Furthermore, the average whisker angle was more posterior and the jaw rested in a
184 more open position in the pre-stimulus period of trials in which the mouse subsequently
185 licked in response to the whisker stimulus independently of context. We also
186 considered whether anticipatory movements of the whiskers and jaw could explain
187 behavioral performance, finding no effect of context or lick reflected in the speed of
188 whisking of the mouse, while jaw speed was significantly increased in the rewarded
189 context (Figure 1J and Figure 1 – figure supplement 1H).

190 We next wanted to assess the combined influence of task parameters such as
191 context, trial index and history, as well as orofacial movement metrics onto task

execution and specifically onto choice in response to whisker trials in the W+ and W- contexts. We trained a gradient boosted tree model (Griffiths et al., 2024) (Figures 1K&L and Figure 1 – figure supplement 1I-L) on concatenated expert sessions including only whisker trials and using uncorrelated features. We used SHAP values (Lundberg and Lee, 2017) to obtain single-trial contributions from each parameter to model outcome. SHAP values can be interpreted as the bias that a single parameter inflicts on predicting outcome toward lick or no lick. Our model reached a cross-validated accuracy of 0.78 on held-out test trials (Figure 1K). Among all model features, context information was the one leading to the strongest accuracy drop in the permutation test, followed by whether or not the previous whisker trial was rewarded, the cumulative number of rewards, and the index of the whisker trial of the block (Figure 1K). Following context transition, mice adapt their response to whisker stimulation already at the first trial of the block, but further improve their choice on the second whisker trial (Figure 1F). To assess if the model could account for this effect, we examined the SHAP value of the parameter “whisker trial in block”, finding a pattern consistent with the mouse behavior capturing both single trial adaptation after context transition and a slower component. Overall, the experimental data and the model indicate that the explicit auditory contexts presented in W+ and W- blocks appear to dominate task performance with additional contributions associated with ongoing behavioral state and reward history.

Distributed cortical areas are involved in task execution

To identify cortical regions involved in task performance, we used an unbiased optogenetic inactivation approach (Guo et al., 2014) using a 1 mm-spaced grid of target locations covering the left hemisphere of the mouse brain. We trained VGAT-ChR2 mice (Zhao et al., 2011) in the context task and, after reaching expert performance, we pseudo-randomly inactivated individual cortical sites in half of the trials by directing a blue light beam to specific grid positions (Figures 2A&B and Figure 2 – figure supplement 1A&B). As a control condition, in the other half of the trials, the beam was directed outside the brain. For each trial type in both W+ and W− contexts, we quantified changes in lick probability relative to these control trials (Figures 2C-E). In catch trials, optogenetic inactivation had little effect on licking behavior in either context (Figure 2C). However, in auditory trials, there was a reduction in lick probability when

225 inactivating auditory cortex and frontal premotor regions, which was similar across
226 contexts (Figure 2D). Finally, in whisker trials, we observed that inactivating primary
227 and secondary whisker somatosensory cortices (wS1 and wS2), as well as anterior
228 premotor regions led to a reduction of lick probability across both contexts (Figure 2E).
229 Interestingly, during whisker trials, inactivation of the tongue–jaw primary
230 somatosensory cortex (tjS1) and the retrosplenial cortex (RSC) increased lick
231 probability with respect to the control condition specifically in W− trials, indicating a
232 context-dependent effect of these two regions (Figure 2E, right panel). In control mice
233 without ChR2 expression, we did not observe any significant changes in lick probability
234 following optogenetic inactivation at any site (Figure 2 – figure supplement 1C&D).
235 Pharmacological inactivation using muscimol injected into wS1, RSC, or the forepaw
236 primary somatosensory cortex gave results consistent with optogenetic inactivation
237 (Figure 2 – figure supplement 1E-G). While lick latency increased during inactivation
238 of frontal areas, presumably correlated with decreased motor function, there was no
239 change in lick latency associated with inactivation of RSC or tjS1 (Figure 2F and Figure
240 2 – figure supplement 1H). Inhibition of tjS1 or RSC therefore does not seem to directly
241 release a motor response, but rather is more likely to act via downstream brain regions.

242 Thus, unbiased optogenetic and targeted pharmacological inactivation revealed
243 several cortical regions critical for the execution of the context task, including wS1,
244 wS2, wM1/2 and ALM, known to be required for whisker-based sensory-to-motor
245 transformations. Furthermore, we identified RSC and tjS1 as key regions which
246 influence the ability of the mouse to adapt its response during whisker trials in a
247 context-dependent manner.
248

249 **Context-dependent flow of activity during sensorimotor transformation**

250 To investigate the spatiotemporal neural dynamics underlying task execution, we
251 recorded calcium activity cortex-wide in transgenic mice expressing jRGECO1a (Dana
252 et al., 2018; Tamura et al., 2025) (Figure 3) or GCaMP6f (Daigle et al., 2018; Harris et
253 al., 2014) (Figure 3 – figure supplement 1), obtaining consistent results. We focused
254 our analyses on the first 120 ms after sensory stimuli, largely preceding the onset of
255 jaw opening (108 ± 24 ms) (Figures 3B&C). We observed comparable patterns of
256 cortical activity in auditory trials across W+ and W- contexts, which was dominated by
257 an early increase in fluorescence in the primary auditory cortex (A1), followed by RSC

(and nearby regions), and, subsequently, activity propagated anteriorly towards a medial part of secondary motor region (including wM1/2), before transitioning to the orofacial motor cortices (including tjS1 and ALM) (Figures 3D&E). In contrast, whisker trials exhibited context-dependent differences in cortical dynamics (Figures 3F&G). Early after stimulus onset, whisker deflection evoked similar activation of primary and secondary whisker somatosensory cortices (wS1 and wS2) in both W+ and W− contexts. However, after ~50 ms post-stimulus, cortical dynamics began to diverge, with increased activity in RSC and wM1/2 in the W+ context compared to the W- context. Importantly, these dynamics were not observed in control mice expressing tdTomato or GFP (Figure 3 – figure supplement 1A&B). To identify the earliest cortical area exhibiting context selectivity, we determined the time point at which each region reached a d′ greater than 2 between W+ and W−. This analysis, performed both on pixel-wise activity maps and on the average fluorescence of target regions, revealed RSC as the first area to show significant context discriminability (Figure 3H).

Together, our results show a context-dependent modulation of activity across the dorsal cortex before the onset of movement. They also point to RSC as a key region in relaying contextual information to other task-relevant cortical regions. The RSC is one of the main cortical outputs from the hippocampal formation (Li et al., 2025; Oh et al., 2014; Todd et al., 2019), which positions it as an interesting candidate to transmit contextual information to downstream cortical regions. To examine axonal projections, we injected AAV vectors into RSC using the coordinates defined in our optogenetic and imaging experiments, finding strong direct connectivity between RSC and frontal motor regions such as secondary motor cortex (wM1/2), consistent with previous anatomical studies (Oh et al., 2014; Yamawaki et al., 2016) (Figure 3 – figure supplement 1C).

Inter-area functional connectivity is modulated by context and upcoming choice

A possible mechanism for the same whisker stimulus to lead to licking or not depending on context could be to alter the functional connectivity between regions involved in the task. We hypothesized that this could be reflected in the correlation of the spontaneous activity during the pre-stimulus baseline period. To test this hypothesis, we computed seed-based correlations between each target area from the grid and each pixel from the image for each 2-s pre-stimulus window. For each seed area, we obtained a

correlation map in both W+ and W- contexts for correct and incorrect trials (Figure 4A and Figure 4 – figure supplement 1). To identify significantly correlated pixels, we compared these correlation maps to null distributions obtained by shuffling entire blocks of trials and thereby preserving task structure (Harris, 2021). Finally, we reduced the obtained correlation map into the grid space which allowed us to build a graph connecting significantly correlated seeds in W- and W+ for correct and incorrect trials (Figure 4B and Figure 4 – figure supplement 1A&B). We found a pattern of significant connectivity between whisker sensory regions, tongue-jaw orofacial regions and RSC with wM1/2 acting as intermediary node in the spontaneous pre-stimulus activity. We observed higher correlation values among orofacial regions, and between whisker motor and orofacial regions in W- compared to W+ in the baseline preceding correct trials. Similarly, there was also an increase in correlation between wS1 and wS2 and between wS2 and wM1/2 in W-. Such contextual modulation of correlation was absent in baseline periods preceding an incorrect trial. This was due to an increase in correlation in incorrect trials in the W+ context (Figure 4B and Figure 4 – figure supplement 1C).

Overall, this resting-state functional connectivity analysis showed reduced correlations between key cortical nodes in baseline periods preceding correct trials in the W+ context. Decorrelated cortical activity patterns can enhance information transmission through increased signal-to-noise ratios (Mukherjee et al., 2021; Poulet and Petersen, 2008; Shahsavarani et al., 2023), and the observed changes in functional connectivity could thus help propagate activity from whisker sensory cortex to frontal executive motor regions in the W+ context.

Optogenetic inhibition drives cortical activity modes predictive of behavior

So far, we have observed that inhibition of RSC prevents switching of behavioral response to the whisker stimulus in the W- context. Importantly, inhibition of RSC in catch or auditory trials did not lead to any changes in performance, indicating that the presence of the context-sensitive stimulus is necessary for the effect of RSC inactivation to become apparent. We have also demonstrated that RSC is the first cortical region to display contextual differentiation in neural activity. Therefore, we investigated whether the behavioral effect of RSC inhibition could be explained by the optogenetically-driven changes in the neural activity patterns after whisker stimulus.

To do so we combined calcium imaging of jRGECO1a and optogenetic inactivation in VGAT-ChR2 double-transgenic mice. We observed a diversity of cortical effects after inhibition during whisker trials (Figure 4C), which were not found in control mice only expressing jRGECO1a (Figure 4 – figure supplement 1D). For instance, inhibition of wS1 (which leads to a strong decrease in lick probability) resulted in widespread decrease in cortical activity, whereas inhibiting wM1/2, which also generated strong decreases in lick probability, concentrated the downstream inhibitory effect among motor areas while leaving the whisker sensory responses intact. These observations indicate a causal directionality of information flow, in which inhibiting each step in the sensorimotor transformation chain propagates selectively forward in the hierarchy. However, inactivation of RSC, which increases lick probability in whisker trials, did not increase activity in wM1/2 or tongue-jaw motor regions, suggesting more complex causal network dynamics. In order to shed light into the underlying patterns of neural activity supporting our observations, we reduced our cortical images into grid space and used PCA to define a low-dimensional space using the mouse averaged control whisker trials, separating lick trials from no-lick trials for each context to preserve the lick dimension (Figure 4 – figure supplement 1E&F). The loadings of PC3 highlighted task-related cortical regions and its timecourse exhibited clear differences comparing lick and no-lick trials. We therefore projected trials with optogenetic inhibition of different cortical areas into this dimension to compare divergence from the control lick and no-lick neural trajectories (Figures 4D&E and Figure 4 – figure supplement 1G). For regions of interest that decreased task performance (wS1, wS2, wM1/2 and ALM), inactivation strongly deviated the trajectories away from the control-lick trajectory, towards no-lick. Only inhibition of RSC and tjS1, regions which led to increased licking, had trajectories that followed that of the control-lick in both contexts. To measure similarity of the opto-evoked neural trajectories with the control-lick trajectory, we computed the angle between these two traces. RSC and tjS1 – areas that increased licking in W- – had smaller angles with respect to the lick trajectories compared to the other regions, which decreased lick probability in all contexts (Figure 4E). This relationship held generally true across all inactivated regions in W+ and W- contexts (Figures 4F&G).

In summary, through combined calcium imaging and optogenetic inactivation, we found causal evidence for directional propagation of sensory signals to frontal

cortex and revealed that RSC drives enhanced licking in W- contexts reflected in specific network subspace dynamics.

Discussion

We developed a behavioral task where mice were able to switch their licking response to identical deflections of the C2 whisker based on an explicitly-presented auditory context (Figure 1). Unbiased optogenetic inactivation mapping of dorsal cortex confirmed key contributions of previously identified regions involved in whisker detection tasks (Chang et al., 2024; Esmaeili et al., 2021; Kwon et al., 2016; Le Merre et al., 2018; Oryshchuk et al., 2024; Sachidhanandam et al., 2013; Yang et al., 2016), as well as revealing an unanticipated role of RSC (Figure 2). Functional imaging of cortical activity with two different genetically-encoded calcium indicators each showed similar spatiotemporal dynamics of whisker sensory processing with the earliest context-dependent divergence in signalling being detected in RSC (Figure 3). Finally, functional connectivity measures and calcium imaging during optogenetic inactivation demonstrated causal contributions of RSC influencing the processing of whisker sensory information (Figure 4). Our results therefore point to an unexpected important contribution of RSC in our context-dependent whisker detection task.

While RSC has traditionally been linked to navigation (Mao et al., 2018, 2017) and vision (Kira et al., 2023; Sit and Goard, 2023; Vedder et al., 2017), recent work has indicated that RSC could also be important for tracking of reward (Hattori and Komiyama, 2022; Sun et al., 2021) and reward locations (Franco and Goard, 2021; Sun et al., 2021; Vedder et al., 2017). RSC is also important for the retrieval of contextual fear memory (Corcoran et al., 2011; Keene and Bucci, 2008; Robinson et al., 2012) and the optogenetic activation of memory-tagged RSC neurons was sufficient to reactivate fear memory (Cowansage et al., 2014). A growing body of evidence suggests that RSC is also involved in learning sensory associations for discrete cues (Todd et al., 2019). Finally RSC circuits are required for associating contextual information with appropriate motor output in a non-navigation task (Franco and Goard, 2021). Taken together with our observations, RSC appears as a key region for the integration of incoming sensory inputs to flexibly adapt a behavioral response according to the ongoing context.

389 In the future, it will be of great interest to investigate how cell-class-specific
390 neuronal activity in RSC might contribute to orchestrating context-dependent interareal
391 communication. Many important questions remain. The circuits signalling whisker
392 sensory information and auditory contextual signals to RSC are currently unknown.
393 Whisker sensory information could be relayed from wS1/2, with anatomical
394 investigations suggesting that some L5IT cells in wS1 and wS2 directly innervate RSC
395 (Liu et al., 2024). Context representations in hippocampus could be relayed to RSC
396 through the direct CA1->RSC pathway (Cenquizca and Swanson, 2007), as well as
397 indirect pathways via subiculum and entorhinal cortex (Sugar et al., 2011). These
398 pathways could lead to the integration of whisker sensation with context in RSC, giving
399 rise to enhanced excitation of a specific relevant subset of neurons in the whisker-
400 rewarded context compared to the whisker-non-rewarded context.

401 An equally important question is how the activity of RSC neurons enables the
402 context-dependent execution of the whisker-dependent detection task. Neurons in
403 RSC project to many other brain regions, including wM1/2 (Figure 4 – figure
404 supplement 1C). In the future, it will therefore be interesting to test the hypothesis that
405 neurons with cell bodies located in RSC and with axons projecting to wM1/2 play a
406 specific role in enabling context-dependent processing of the whisker stimulus. Key
407 experiments will include: i) to measure the activity of individual neurons in RSC
408 retrogradely-labelled from wM1/2 and/or image axons in wM1/2 originating from
409 neurons in RSC; ii) to inhibit RSC->wM1/2 signalling via inhibitory opsins expressed in
410 retrogradely-labelled neurons in RSC, for example with stGtACR2 (Mahn et al., 2018),
411 and/or optogenetic presynaptic inhibition of RSC axons in wM1/2, for example using
412 PdCO (Wietek et al., 2024); and iii) to stimulate RSC neurons projecting to wM1/2 to
413 examine whether the auditory context can be substituted by optogenetic stimulation of
414 specific subsets of RSC neurons.

Methods

Animals

All procedures were approved by the Swiss Federal Veterinary Office (License number VD-3769) and were conducted in accordance with the Swiss guidelines for the use of research animals. We used both male and female adult mice of at least 5 weeks at the time of surgery. For behavior only and pharmacological inactivation experiments we used wild-type mice. For calcium imaging experiments we used two subsets of mice: Thy1-jRGECO1a mice [Tg(Thy1-jRGECO1a)GP8.20Dkim/J, JAX: 030525] (Dana et al., 2018), which express a red shifted calcium indicator broadly across cortical regions, and Rasgrf2-dCre mice [B6;129S-Rasgrf2 <tm1(cre/folA)Hze>/J, JAX: 022864] (Harris et al., 2014) crossed with Ai148 mice [B6;Ai148(TIT2L-GC6f-ICL-tTA2)-D, JAX: 030328] (Daigle et al., 2018), which express the green fluorescent calcium indicator GCaMP6f specifically in excitatory layer 2/3 neurons. To test the effect of optogenetic stimulation of inhibitory neurons, we used VGAT-ChR2 mice [B6.Cg-Tg(Slc32a1-COP4*H134R/EYFP)8Gfng/J, JAX: 014548] (Zhao et al., 2011). For simultaneous calcium imaging and optogenetic manipulations we crossed VGAT-ChR2 mice with Thy1-jRGECO1a mice. For GCaMP calcium imaging control experiments, we used GAD67-GFP mice [CR.Cg-Gad1tm1.1Tama/Rbrc, MGI:3590301] (Tamamaki et al., 2003), which have a similar level of green fluorescence. For jRGECO1a calcium imaging control experiments, we used PV-Cre mice [B6;129P2-Pvalbtm1(cre)Arbr/J, JAX: 008069] (Hippenmeyer et al., 2005) crossed with R26_LSL_tdTomato mice [B6.Cg-Gt(ROSA)26Sor<tm9(CAG-tdTomato)Hze>/J , JAX: 007909] (Madisen et al., 2010), which have a similar level of red fluorescence.

Implantation of headpost and skull preparation

Mice were first implanted with a metal head-post under isoflurane anesthesia (1.5-2.5 % isoflurane). Before the start of the surgery, we injected carprofen (7.5 mg/kg at 1.5 mg/ml, subcutaneous) for general analgesia, and a mix of lidocaine and bupivacaine below the scalp as local analgesic. An ocular ointment (Vita-Pos, Pharma Medica AG, Switzerland) applied over the eyes prevented them from drying during the surgery, and a solution of povidone-iodine (Betadine, Mundipharma Medical Company, Bermuda)

447 was applied for skin disinfection before incision. We monitored body temperature
448 throughout the surgery and it was maintained at 37°C with a heating pad (ThermoStar,
449 Intellibio, France). After excising the scalp with surgical scissors to expose the skull,
450 we thoroughly cleaned it with cotton buds and a scalpel blade to remove the periosteal
451 tissue. After further disinfection with Betadine, the skull was dried with cotton buds and
452 made optically clear using a thin layer of super glue applied over the dorsal part of the
453 skull (Loctite super glue 401, Henkel, Germany). We then glued a custom-made head
454 fixation implant above the right hemisphere, and further secured it with self-curing
455 denture acrylic (Paladur, Kulzer, Germany or Ortho-Jet, Lang, USA). Finally, a second
456 thin layer of the glue was applied homogeneously on the left hemisphere to ensure a
457 smooth and equally transparent field of view. Particular care was taken to ensure that
458 the left hemisphere of the dorsal cortex was free of denture acrylic and only covered
459 by super glue for optical access. This intact, transparent skull preparation was used to
460 perform intrinsic optical signal (IOS) imaging, widefield imaging experiments, and opto-
461 inhibition screening. Mice were returned to their home cages and ibuprofen (Algifor
462 Dolo Junior, Verfora SA, Switzerland) was added to the drinking water for three days
463 after surgery.
464

465 **Behavioral task and training curriculum**

466 We trained head-fixed, water-restricted mice to perform a context-dependent
467 multisensory detection task. During the behavioral experiments, all whiskers were
468 trimmed except for the C2 whisker, and the mice were water restricted to 0.9-1.2 mL
469 of water/day (depending on the initial body weight). Mice were trained daily with one
470 session per day, their weight and general health status were carefully monitored using
471 score sheets. Mice were habituated to be head-fixed to a metal post with their head
472 held in a 30-degree angle. During the first session, mice were also habituated to licking
473 from a water spout positioned on their right side which delivered 5 μL of water in
474 response to some licks. Next, we trained them in an auditory detection task for three
475 to five days during which licking in a 1 s response window after the auditory cue (10
476 ms, 10 kHz tone of 74 dB embedded in the continuous background white noise of 80
477 dB) was rewarded. Inter-trial interval was uniformly sampled between 6 and 10 s
478 including a final 2 to 5 s no-lick window during which the mice were required not to lick
479 for the trial to be initiated. Once the mice showed clear detection of the auditory cue,

480 we introduced for two to three days a C2 whisker deflection (a 25 mT magnetic pulse
481 driven by a 3 ms cosine pulse sent into an electromagnetic coil positioned under the
482 head of the mouse and acting upon a small metal particle attached to the C2 whisker),
483 which like the auditory cue was also rewarded if the mice licked within 1 s following the
484 stimulus. Mice were then trained in a block-based contextual task. Contextual
485 information was provided by alternating pink and brown noise instead of white noise in
486 the background. Each mouse was randomly assigned a whisker-rewarded context
487 (W+) at the beginning of training. Pink and brown background noise alternated every
488 block of 20 trials, and was continuously present and available to the mice. Within each
489 20-trial block, mice received 8 whisker trials, 4 auditory trials and 8 catch trials
490 presented pseudo-randomly. Mice were trained in this paradigm until they reached
491 expert level. To determine expert level, we computed a contrast value for each block
492 of context apart from first and last ones. It was defined as the average of the absolute
493 difference in the whisker hit rate between one block and the two surrounding blocks.
494 For each session we obtained a distribution of contrast values and compared it to a
495 threshold of 0.375, which essentially requires mice to respond differently for at least
496 7/16 possible whisker trials between blocks throughout the entire session. Sessions
497 with significantly above threshold average contrast values were classified as expert.
498 For each session we computed the context discriminability using Cohen's d.

499

500 **Video tracking and pose estimation**

501 Simultaneously with behavioral training and imaging, we recorded mouse orofacial
502 movements using two cameras (DMK 37BUX273, The Imaging Source) positioned
503 above and on the side of the mouse face with pixel size calibrated to real distance (top
504 camera 24 pixels/mm, side camera 28 pixels/mm). Acquisition was freely running at
505 either 100 Hz or 200 Hz and we recorded timestamps of each image relative to session
506 start-time. We trained a network using the behavioral pose estimation software
507 DeepLabCut (Mathis et al., 2018) (v3.0.0rc6) to track different body parts of the
508 orofacial region. We labelled 940 frames uniformly extracted from 47 sessions in 24
509 mice for each camera view. We trained our network using 95% of the data as training
510 fraction, and a ResNet 50 with a batch size of 8 (default parameters). After training, we
511 obtained a train error of 3 pixels at 60% likelihood cutoff, and a test error of 3.71 pixels
512 for the same cutoff value in the side view camera. Evaluation results were similar for

513 the top view camera, with 3.8 pixels of error in the train dataset, and 3.75 pixels for the
514 test dataset at 60% likelihood cutoff.
515

516 **Optogenetic inactivation**

517 For optogenetic inactivation experiments, a multimode custom patch fiber (0.22 NA,
518 105 μm diameter core, FG105UCA, Thorlabs, USA) attached to a 473 nm laser source
519 (S1FC473MM, Thorlabs, USA) was used to direct a laser beam into a set of galvo-
520 galvo scan mirrors (GVS202, Thorlabs, USA). We designed a grid of 39 points
521 separated by 1 mm covering the left dorsal cortex, and calibrated the grid to bregma.
522 Due to the large number of stimulation points, we further randomly divided the total
523 grid into three subgrids, which each mouse experienced over multiple sessions in a
524 randomized rotating schedule. In fifty percent of the trials, we randomly directed the
525 laser beam to a subgrid point to excite ChR2 expressing neurons with a train of 5 ms
526 square pulses at 50 Hz from 10 ms before the stimulus to 1 sec after. The other fifty
527 percent of trials were non-stimulated trials, in which we directed the laser beam outside
528 the brain. We iterated over subgrid points over a single session and over subgrids over
529 multiple sessions (days).
530

531 **Pharmacological inactivation**

532 We performed muscimol inactivation on mice trained in the context-dependent
533 detection task after they reached expert level for at least two consecutive days. On the
534 day before injection, after the training session, we performed a small craniotomy above
535 the targeted region. We used the intrinsic optical signal to target the C2 column of the
536 whisker primary sensory cortex (C2-wS1), the forepaw primary sensory cortex
537 coordinates were estimated 1.5 mm anterior and 1.5 mm medial compared to C2-wS1,
538 the retrosplenial cortex coordinates were 1.5 mm posterior to bregma and 0.5 mm
539 lateral from the midline. On the inactivation day, we injected 100 nL per injection depth
540 of muscimol 5 mM diluted in Ringer (or Ringer alone in control experiments) at 200,
541 400, 600 and 800 μm below the pia. We started the behavioral session fifteen minutes
542 after the last injection. We performed up to four injections (muscimol and/or control)
543 per mouse separated by at least one day with a normal behavioral session.
544

545 **Calcium imaging**

546 We collected cortex wide imaging data from 4 mouse lines expressing different
547 fluorescent proteins: i) mice expressing the red calcium indicator jRGECO1a; ii) mice
548 expressing tdTomato as a calcium insensitive red fluorophore control for jRGECO1a;
549 iii) mice expressing the green calcium indicator GCaMP6f in layer 2/3 excitatory
550 neurons; and iv) mice expressing GFP as a calcium insensitive green fluorophore
551 control for GCaMP6f. We excited jRGECO1a (and tdTomato) using 563 nm light (19.2
552 $\mu W/mm^2$ on the cortical surface; 567 nm LED, SP-01-L1, Luxeon, Canada; 563/9 nm
553 BrightLine HC bandpass filter, Semrock, USA). Red emission light was separated from
554 excitation light using a dichroic mirror (Beamsplitter T 588 LPXR, Chroma, USA) and
555 bandpass filtered (645/110 ET Bandpass, Semrock). To excite GCaMP6f (and GFP),
556 we directed blue light from a 488 nm LED (M490L4, Thorlabs), narrowband filtered at
557 488 (488/6 BrightLine HC, Semrock, USA). Emitted light was separated from excitation
558 light using a beamsplitter (T 495 LPXR, Chroma, USA) and bandpass filtered (525/50
559 BrightLine HC, Semrock, USA). Images were taken using a 16-bit monochromatic
560 scientific Complementary Metal Oxide Semiconductor camera (sCMOS, Hamamatsu
561 Orca Flash 4.0 v3, Hamamatsu Photonics, Japan) coupled in face-to-face tandem to
562 an objective and imaging lens (Nikkor 50 mm f/1.2, Nikon, Japan; 50 mm video lens,
563 Navitar, USA, respectively). We collected 256 x 320 pixel-sized images of the dorsal
564 cortex of the brain at 100 Hz with a 10 ms exposure time using the
565 "SynchronousTrigger" mode.

566 For combined calcium imaging and optogenetics, we collected 256 x 320 pixel-
567 sized images of the dorsal cortex of the brain at 50 Hz with a 2.5 ms exposure time in
568 the "EdgeTrigger" mode. Imaging frames were interleaved to the optogenetic pulses
569 to minimize optolight contamination.

570

571 # Quantification and data analysis

572 **Computation of $\Delta F/F_0$**

573 To compute relative changes in fluorescence over time, for each pixel in the widefield
574 video, we computed the 5th percentile of the distribution of session-wide values and
575 used that as F_0. We then computed the moment-by-moment difference between the
576 fluorescent values and F_0 and divided by F_0. In Figures 3&4 and Figures 3&4

supplement 1, calcium data was further processed by subtracting the average of the 250 ms prior to stimulus onset to the stimulus aligned images for each trial before averaging.

Behavioral kinematics

After obtaining the session-wide pose estimation from DeepLabCut, we computed body part kinematics prior to integration in NWB datafiles.

We computed the opening of the jaw as the vertical distance from a reference point determined by the 5th percentile of the entire jaw trace (after filtering at 50% likelihood cutoff). Jaw speed was then computed as the absolute of the first derivative of the jaw opening traces.

To compute the whisker angle, we calculated the arc cosine of the dot product between the vector formed by the metal particle used to deliver the whisker deflections and the base of the whisker, with the vector crossing the midline of the mouse (computed by the median position over the session of the tip and base of the nose) divided by the norm:

$$\theta = cos^{-1}\left(\frac{v_1 \cdot v_2}{|v_1| \cdot |v_2|}\right)$$

where v1 = ($X_{particle} - X_{whisker_base}$, $Y_{particle} - Y_{whisker_base}$), and v2 = (median($X_{nose\ tip}$) – median($X_{nose_base}$), median($Y_{nose_tip}$) – median($Y_{nose_base}$)). Finally, this angle was rotated such that a fully protracted whisker (parallel to the body) would be 180 degrees and a fully perpendicular whisker to the midline was 90 degrees. As with the speed of jaw movements, whisker speed was computed as the absolute of the first derivative of the whisker angle.

In addition, we computed the area of the pupil as the surface of the polygon with the four points tracking the top, right, bottom, and left of the pupil as vertices. In order to be computed, all four points were required to have a likelihood bigger than 0.5 for each given point.

607 **Seed correlations**

608 After extracting the minimal common quiet window period before stimulus onset from
609 each trial (2 s quiet window), we progressively iterated over regions of interest (wS1,
610 S2, wM1, RSC, ALM, tjM1, and tjS1) and pooled the pixels inside the 1 mm circle
611 centered on the coordinates of the optogenetic grid inhibition. As such we obtained a
612 source matrix for each ROI being (trials x frames), and a target tensor for the entire
613 session being (trials x frames x pixels). Then we iterated over pixels to compute the
614 trial-by-trial Pearson's zero lag correlation between the ROI and each pixel.

615 To generate a null distribution while preserving general structure of the session,
616 we shuffled 1,000 times entire blocks by randomly swapping the block identity, which
617 preserved the within-block structure. This shuffling method is stricter than simply
618 shuffling all trials, since it would preserve slow components of the block. We
619 considered pixels significantly correlated to the seed if the correlation coefficient of that
620 pixel was on average larger or equal than 1.8 times the standard deviation of the null
621 distribution.

622

623 **Principal component analysis**

624 To compute the low dimensional space onto which to project our simultaneous
625 widefield imaging and optogenetic inactivation data, we first extracted the widefield
626 images for the time period of 300 ms surrounding a whisker trial and reduced them to
627 grid space by pooling the pixels within a 1 mm diameter circle centered on locations
628 from our optogenetic grid. We then extracted control stimulation trials (where light is
629 projected outside the brain, ~50% of total trials), and computed the total average $\Delta F/F_0$
630 by first averaging across each individual mouse pseudosession and then across mice.
631 Next, we computed the principal components of the matrix that has as columns the
632 optogrid ROI $\Delta F/F_0$, and as rows a multi-index of time, lick, trial type (whisker or catch),
633 and context. Preserving the lick dimension allows us to investigate the differences of
634 lick trials vs no-lick trials. We then recomputed the mouse average matrix by averaging
635 by trial type within each pseudosession regardless of lick or no lick (thus computing
636 the weighted average calcium responses best mimicking the effect of our inhibition in
637 Figure 2). Then, we projected the mouse average data using the same set of weights
638 obtained by projecting the control trials.

Gradient boosted decision tree model

Behavioral data from all expert sessions were concatenated in a single table. One single session was randomly chosen to be used as a held-out test session. Then, data were split into a 67% train set and 33% test set, with a stratification strategy to ensure that the proportion of the binary outcome was the same in both train and test sets. The target value was whether the animal licked or not in response to the whisker stimulus. A Gradient Boosted Tree (GBT) model was fitted on the data using the package XGBoost (Chen and Guestrin, 2016).

Gradient Boosted Trees are ensemble learning methods that build models sequentially, where each tree is a weak decision tree classifier trained to predict the outcome of a trial. The key principle is that each subsequent tree is trained to correct the prediction errors made by the previous trees, with the final prediction being the weighted sum of all tree predictions. This iterative approach allows the model to progressively improve its performance by focusing on the most challenging cases. GBT models have been demonstrated to be particularly effective for tabular data, often outperforming nonlinear neural network-based classifiers (Grinsztajn et al., 2022). Furthermore, this approach has proven valuable for modeling behavioral data as it can capture non-linear relationships as well as complex interactions that traditional linear models fail to capture (Griffiths et al., 2024).

Hyperparameter tuning was performed using Bayesian optimization implemented in Optuna (Akiba et al., 2019). The optimization minimized binary log loss for classification tasks using a holdout validation approach, where the training data was split 80/20 into training and validation sets. Early stopping with 100 rounds was applied to prevent overfitting during model training. The search space included 12 hyperparameters. The best hyperparameters were then used to train the GBT model on the full training set, using binary log loss. Balanced accuracy was then computed on the test set. To interpret the trained GBT model and gain a better understanding of how each feature contributes to the prediction, we used SHapley Additive exPlanations (SHAP) analysis (Lundberg and Lee, 2017). In short, SHAP values, originating from cooperative game theory, provide a mathematically rigorous method for attributing the contribution of each feature to a model's prediction.

Statistics

For statistics we used parametric tests and correction for multiple comparisons using the Bonferroni method.

Figure-specific analysis methods

Figures 1C-E: These panels describe the average probability of licking to different trial types of expert mice in the context task. Each dot represents a mouse, obtained by first averaging trials within a session then across sessions for each mouse. Population average is obtained by further averaging over mice, and error bars show the 95% confidence interval of the population mean.

Figure 1F: This panel represents the speed of switching behavior after context transition. Single mice are not shown; each dot represents the population average; error bars show the 95% confidence interval of the population mean.

Figure 1G: Summary plot representing the speed of switch in the last vs first trial after context switch. Each dot represents a mouse at whisker trial -1 and +1 extracted from Figure 1F.

Figure 1H: Same as Figure 1F but represented as time around context transition in which the last/first whisker trial occurs. We selected for each session the first and last whisker trials of each block around context transition (i.e. excluding first whisker trial of the first block and last whisker trial of the last block), this yielded approximately 10 'first' whisker trials and 10 'last' whisker trials for each session. We then assigned a label to each of these trials according to which of the 10-s bins around context transition it belonged. We repeated the same process over all sessions. For each 10-s time bin we defined the lick probability as the number of trials with lick divided by the total number of trials in this time bin.

Figures 1I-J: Quantification of postural and movement changes according to context and lick. We extracted movement traces for jaw opening, whisker angle and pupil area from the NWB files. Pupil area was computed as the surface of the polygon that has as vertices 4 points surrounding the pupil (top, bottom, left and right), and only computed for timestamps in which the likelihood values of all vertices were above 50%.

We computed whisker and jaw speed as the absolute of the derivative of the jaw and whisker traces respectively, times the frame rate. Next, we filtered the body parts using an adaptive threshold of 80% likelihood for whisker, 60% for jaw, and 50% for pupil and any body part that kept less than 70% of the data points after filtering over the entire session was discarded from analysis. We then extracted the two-second arrays corresponding to the pre-stimulus imposed quiet window and averaged them within sessions, then within mouse preserving context and lick categories. We used the population array to compute statistics using paired t-tests. We computed paired effect size as the absolute difference between means divided by the standard deviation of the individual differences: $d' = |\mu_1 - \mu_2| / \sigma_{x_1 - x_2}$, where μ signifies the mean and σ the standard deviation.

Figure 1K: For our Gradient Boosted Decision Tree model, we show the results of the permutation test with scikit-learn (Pedregosa et al., 2011) used to validate which features have the largest contributions to model performance. In this procedure, the feature importance was assessed by randomly shuffling each feature 10,000 times while keeping all other features intact. For each permutation, the model's performance was evaluated on the test set, and the decrease in balanced accuracy was recorded.

Figure 1L: In this panel, we show the interaction between the SHAP values of the whisker trial in block versus the whisker trial in block as it is used in Figure 1F. To compute the SHAP values, we used the Python SHAP package (Lundberg and Lee, 2017) with the interventional feature perturbation method. This method treats each feature's contribution as if we were experimentally manipulating that feature while holding others constant, which is particularly important when features are correlated or interdependent. To achieve this, we randomly sampled 100 trials from the training data to serve as a background dataset representing the typical distribution of our data. For each prediction, the interventional method calculates SHAP values by replacing each feature's value with values from the background dataset while keeping other features fixed. This process estimates the expected change in model output when intervening on a specific feature. The SHAP value for a feature in a given trial represents the difference between the model's prediction with the actual feature value and the expected prediction when that feature is marginalized over the background distribution. Positive SHAP values indicate that a feature increases the probability of licking for that specific trial, while negative values indicate a decrease. The violin plots represent the

735 distributions of SHAP values for each whisker trial in block, and context, from single
736 trials included in the model.

737 **Figures 2C-E:** Summary plots representing the changes in lick probability with respect
738 to control stimulation in our optogenetic manipulation experiments. Given that our
739 protocol for optogenetic inactivation completes a grid over the course of ~3 sessions,
740 we considered all the sessions for each mouse as a single pseudosession. For each
741 mouse, context, trial type and inactivation coordinates, we computed the probability of
742 licking (see also Figure 2 – figure supplement 1A&B) and subtracted from it the
743 probability of licking in our control stim condition (where light is projected outside the
744 brain), thus obtaining for each grid coordinate a ∆P(Lick) for each mouse. To estimate
745 the effect size of inactivation, we shuffled the labels of entire blocks of trials (keeping
746 trial order and structure, but shuffling block identity) and recomputed ∆P(Lick) in the
747 same way to obtain a null distribution. We then computed the d' between the null
748 distributions of ∆P(Lick) and the observed distribution.

749 **Figure 2F:** Cortical maps representing the changes in lick latency recorded from the
750 piezo sensor attached to the water spout. We computed for each mouse the average
751 of the spout contact time in response to auditory trials in both contexts and to whisker
752 trials in W+ for each inhibition location and subtracted the averaged spout contact time
753 from control trials. We further averaged this distribution of change in spout contact time
754 over mice. This resulted in the grid maps shown in the top row. To provide an estimate
755 of the variance we computed for each inhibition site the distance between the
756 distribution of spout contact time to the one obtained in control trials. This resulted in
757 the grid maps shown in the bottom row.

758 **Figure 3B:** Average jaw opening trace after whisker onset. As in Figures 1I&J, we
759 extracted movement traces for jaw opening from the NWB files and filtered them at a
760 60% likelihood threshold. We extracted jaw opening traces centered at the time of
761 whisker delivery for correct trials (i.e. licks to whisker in W+ and no licks in W-) and
762 centered them by subtracting the average jaw opening value 250 ms before stimulus
763 onset. We averaged the jaw traces first within session and then across sessions for
764 each mouse before computing the population average response across mice. The
765 shaded region represents 95% confidence intervals computed over mice.

766 **Figure 3C:** Average reaction times for each mouse computed from the jaw traces in
767 Figure 3B. For each mouse average jaw opening trace we computed the d' between

768 the distribution of jaw opening values at each timepoint with the average of the 250 ms
769 before stimulus onset. We determined the onset of movement by selecting the first
770 point after whisker stimulus with a d' bigger or equal to 1.

771 **Figure 3D:** To map sensory-evoked activity onto the grid of coordinates, we manually
772 drew a 1 mm circular ROI centered on the peak response to whisker or auditory trials
773 for each imaging session. We then averaged the center of mass of wS1, wS2 and A1
774 first across sessions for each mouse and then across mice. This averaged center of
775 mass is represented by small stars on the grid.

776 **Figures 3E&F:** Population average stimulus-evoked calcium dynamics across the
777 cortex (left) and from selected regions of interest (right). We first realigned activity
778 (normalized as $\Delta F/F_0$) to trial onset for each session and subtracted the baseline
779 activity (defined by the average value of the 50 ms preceding the trial) in a trial-based
780 manner. We then averaged this normalized activity over trials within each session. We
781 further averaged over sessions for each mouse and finally over mice. The d' rows show
782 the distance between distribution of mouse averages between W+ and W- for each
783 pixel (6 values for each context for each pixel). For the ROI timecourses, the error bars
784 shadowing the population averages show the 95% confidence interval of the
785 population mean.

786 **Figure 3G:** Representation of similarity of responses across contexts or trial types. We
787 used the mouse averaged response to auditory and whisker trials in W- and W+ to
788 detect the maximal $\Delta F/F_0$ value in a time window from 50 ms to 120 ms after stimulus
789 delivery. We show the correlation of maximal $\Delta F/F_0$ in this time window between the
790 two sensory modalities in each context or between the two contexts for each sensory
791 modality. Each dot represents a mouse, each color represents a target region.

792 **Figure 3H:** (Left) Map representing the latency to context divergence for each pixel,
793 defined as the time of the first frame at which the d' (shown in Figure 3F bottom row)
794 exceeds a value of 2. Since d' can be sensitive to low variance time points, the first 20
795 ms after the stimulus delivery - before any response in both contexts - were excluded
796 from the search. (Right) Ranking of regions of interest showing the earliest contextual
797 divergence: same as Left panel, but with d' computed from the ROI averages shown
798 on the right in Figures 3E&F.

Figures 4A&B: Summary results of the seed correlation analysis. For each imaging session, we extracted the $\Delta F/F_0$ widefield data in the 2-s quiet window preceding each trial start. We also extracted the same time periods for the pixel averaged $\Delta F/F_0$ traces corresponding to the area under a given optogenetically defined ROI to obtain our seeds and computed the zero-lag Pearson correlation coefficient between the seed and each pixel in the widefield image, for each trial independently. We focused our analysis to the seed coordinates that showed effects of inactivation in whisker trials (wS1, wS2, RSC, wM1/2, ALM, tjM1, and tjS1). We also shuffled entire blocks of trials (to preserve session structure) by shuffling the block id's and recomputed the zero-lag Pearson correlation coefficient 1,000 times to obtain a null distribution. For each pixel, trial, and session we then computed the number of standard deviations away from the shuffle distribution that a given pixel correlation coefficient was, which allowed us to compute an estimate of significance. We then averaged first within session, then over sessions for each mouse the correlation maps (reconstructed into widefield cortical maps) maintaining the context, and correct vs incorrect categories. To construct connectivity maps, we masked the pixels that had on average, for each category, a correlation coefficient larger or equal to 1.8 times the standard deviation of the shuffle distribution, which under consideration of a gaussian distribution corresponds to the 95th percentile. Then, we reduced the masked coefficient cortical map into optogenetic grid space by averaging the masked correlation coefficients of the pixels under the area corresponding to the 1 mm circle centered on optogenetic coordinates. Finally, we connected the graph by cross validating which nodes of the optogenetic coordinates were significantly correlated (>=1.8 times the standard deviation of the null distribution) for each seed. Once we had a connected graph for each context, and correct vs incorrect trial types, we subtracted the r values for each connected pair to obtain Δr maps. We also tested for significance of the difference by means of a related t-test corrected for multiple comparisons using Bonferroni correction, and computed the effect size of the difference by computing the Cohen's d for related samples as explained above: $d' = |\mu_1 - \mu_2|/\sigma_{x_1 - x_2}$. Each plot in Figures 4A&B corresponds to the average correlation r values across mice, and the line thickness in the Δr maps in Figure 4B increases with d' such that thinnest colored lines correspond to a d' of 0.8 and max thickness is capped at 2. If the correlation difference between two points has a d' below 0.8 this line is plotted in gray.

832 **Figure 4C:** Description of the combined widefield and optogenetic setup and example
833 image sequences. To obtain average post-optogenetic stimulation widefield time
834 courses we averaged the trial start aligned widefield $\Delta F/F_0$ arrays for each session,
835 context, and optogenetic coordinate point. Then we averaged over sessions for each
836 mouse and finally across mice to obtain mouse average widefield maps.
837 **Figure 4D and Figure 4 – figure supplement 1E-H:** Results of the dimensionality
838 reduction analysis on the combined widefield and optogenetics data. To compute low
839 dimensional projections of our simultaneous optogenetic and widefield experiments we
840 first separated the control trials (where light was directed outside the brain) from the
841 optostim trials. We extracted the optogenetic grid space widefield images (obtained by
842 averaging pixels inside the 1 mm circle centered to each coordinate in our optogenetic
843 grid) aligned to trial onset in whisker and catch trials. We then computed the population
844 average control trials by averaging first all the control trials in the pseudosession
845 generated for each mouse, and then averaging across mice while preserving the
846 context, trial type, lick, and timestamp categories, as well as the identity of each
847 coordinate point. We standardized our dataset by fitting and then transforming using
848 the StandardScaler from sklearn, and pivoted to obtain a matrix with the optogenetic
849 grid coordinates as columns and context, trial type, lick, and timestamps as rows before
850 computing the 15 first principal components of this matrix using PCA. In Figure 4 -
851 figure supplement 1E&F, we plot the variance explained and the weights mapped back
852 into optogenetic grid coordinates for the first 3 components. Once we obtained our
853 principal components, we repeated the same process for the stim trials, but in this
854 case, we preserved mouse identity and coordinate of the optogenetic stimulation,
855 hence obtaining a matrix that had as columns the optogenetic grid coordinates, and
856 mouse identity, optogenetic stimulation coordinate, context, trial type, and timestamp
857 categories as rows. This way, our average projections will contain the weighted
858 average over the lick axis for the stim conditions and will reflect better the observations
859 in the average optogenetic inhibition results. We standardized the stim matrix using
860 the same parameters to scale the control matrix, then projected onto the same low
861 dimensional space using the control principal components. We then aggregated over
862 mice for each context, optogenetic stimulation coordinates, and principal component
863 to obtain the low dimensional projections for each PC as found in Figure 4D and Figure
864 4 - figure supplement 1H. Then, we plotted the control-lick and control-no-lick

projections for each context, and the projection obtained from the optoinhibition trials, with shaded area representing 95% confidence interval computed over mice.

Figures 4E-G: Summary plots representing the difference between the low dimensional projections in control-lick versus photoinhibition. After obtaining the low dimensional projections for the control and stim mouse average trials, we computed the angle between the stim traces for each mouse and the average control-lick trace to estimate the divergence from lick. We computed the angle in radians by obtaining the cosine of the dot product between the control-lick and stim vectors, divided by the norms, and then convert it to degrees:

$$\theta = cos^{-1}\left(\frac{v_1 \cdot v_2}{|v_1| \cdot |v_2|}\right)$$

Figure 4E contains a bar graph representation of the angles for the selected subset of optogenetic grid coordinates that show effects in Figure 2. Each dot represents the angle between control-lick and optoinhibition low dimensional projection in PC3 for each context, and error bars represent 95% confidence intervals. Figures 4F&G(left) contain the mouse average angle between control-lick and optoinhibition PC3 projections for each context respectively for each optogenetic stimulation coordinate. Figures 4F&G(right) show the linear regression between the value of the angles in PC3 for each point and the evoked changes in lick probability for the subset of mice that we conducted the simultaneous optogenetic and widefield experiments.

Data availability

For each imaging session, imaging data, behavioral data, cortical region contours and calcium traces, were combined into a single NWB file. NWB offers a common format for sharing and analyzing neurophysiology data (Rübel et al., 2022). Subsequently, we developed open-source Python scripts to analyze data in the NWB format. The full dataset in NWB format will be available on the DANDI archive and processed data will be available via Zenodo at https://doi.org/10.5281/zenodo.17424306.

Code availability

Code for data acquisition and behavior control is available on github (behavior GUI repo). All the code used to preprocess and convert the data into NWB format is

available on github (NWB converter repo), all the code used for data analysis is available on github (NWB analysis repo), Cicada is available on gitlab. The Python code used for analyses will also be available via Zenodo at https://doi.org/10.5281/zenodo.17424306.

Acknowledgements

We thank the members of the Petersen laboratory for helpful discussions. This work was supported by grants from the Swiss National Science Foundation: 31003A_182010 (C.C.H.P.), 310030_219343 (S.C. and C.C.H.P.) and TMAG-3_209271 (C.C.H.P.).

Author contributions

P.B., R.F.D., S.C. and C.C.H.P. conceptualized the study; P.B., R.F.D., A.B. and A.R. wrote the data acquisition codes. P.B. and R.F.D. performed all animal experiments and constructed the database. R.F.D. and L.S. performed the anatomy experiments. P.B., R.F.D., and J.L. analyzed the data. P.B., R.F.D., S.C. and C.C.H.P. wrote and edited the manuscript, with comments from all authors; S.C. and C.C.H.P. acquired funding and provided overall supervision.

Declaration of interests

The authors declare no competing interests.

References

Akiba T, Sano S, Yanase T, Ohta T, Koyama M. 2019. Optuna: A Next-generation Hyperparameter Optimization FrameworkProceedings of the 25th ACM SIGKDD International Conference on Knowledge Discovery & Data Mining, KDD '19. New York, NY, USA: Association for Computing Machinery. pp. 2623–2631. doi:10.1145/3292500.3330701

Allen WE, Chen MZ, Pichamoorthy N, Tien RH, Pachitariu M, Luo L, Deisseroth K. 2019. Thirst regulates motivated behavior through modulation of brainwide neural population dynamics. *Science* **364**:253. doi:10.1126/science.aav3932

Asaad WF, Rainer G, Miller EK. 1998. Neural Activity in the Primate Prefrontal Cortex during Associative Learning. *Neuron* **21**:1399–1407. doi:10.1016/S0896-6273(00)80658-3

Banerjee A, Parente G, Teutsch J, Lewis C, Voigt FF, Helmchen F. 2020. Value-guided remapping of sensory cortex by lateral orbitofrontal cortex. *Nature* **585**:245–250. doi:10.1038/s41586-020-2704-z

Birrell JM, Brown VJ. 2000. Medial Frontal Cortex Mediates Perceptual Attentional Set Shifting in the Rat. *J Neurosci* **20**:4320–4324. doi:10.1523/JNEUROSCI.20-11-04320.2000

Cenquizca LA, Swanson LW. 2007. Spatial organization of direct hippocampal field CA1 axonal projections to the rest of the cerebral cortex. *Brain Res Rev* **56**:1–26. doi:10.1016/j.brainresrev.2007.05.002

Chang Y-T, Finkel EA, Xu D, O'Connor DH. 2024. Rule-based modulation of a sensorimotor transformation across cortical areas. *eLife* **12**:RP92620. doi:10.7554/eLife.92620

Chen S, Liu Y, Wang ZA, Colonell J, Liu LD, Hou H, Tien N-W, Wang T, Harris T, Druckmann S, Li N, Svoboda K. 2024. Brain-wide neural activity underlying memory-guided movement. *Cell* **187**:676-691.e16. doi:10.1016/j.cell.2023.12.035

Chen SX, Kim AN, Peters AJ, Komiyama T. 2015. Subtype-specific plasticity of inhibitory circuits in motor cortex during motor learning. *Nat Neurosci* **18**:1109–1115. doi:10.1038/nn.4049

Chen T, Guestrin C. 2016. XGBoost: A Scalable Tree Boosting SystemProceedings of the 22nd ACM SIGKDD International Conference on Knowledge Discovery and Data Mining, KDD '16. New York, NY, USA: Association for Computing Machinery. pp. 785–794. doi:10.1145/2939672.2939785

Chen T-W, Li N, Daie K, Svoboda K. 2017. A map of anticipatory activity in mouse motor cortex. *Neuron* **94**:866-879.e4. doi:10.1016/j.neuron.2017.05.005

Chevée M, Finkel EA, Kim S-J, O'Connor DH, Brown SP. 2022. Neural activity in the mouse claustrum in a cross-modal sensory selection task. *Neuron* **110**:486-501.e7. doi:10.1016/j.neuron.2021.11.013

Cole N, Harvey M, Myers-Joseph D, Gilra A, Khan AG. 2024. Prediction-error signals in anterior cingulate cortex drive task-switching. *Nat Commun* **15**:7088. doi:10.1038/s41467-024-51368-9

Condylis C, Lowet E, Ni J, Bistrong K, Ouellette T, Josephs N, Chen JL. 2020. Context-dependent sensory processing across primary and secondary somatosensory cortex. *Neuron* **106**:515-525.e5. doi:10.1016/j.neuron.2020.02.004

Corcoran KA, Donnan MD, Tronson NC, Guzmán YF, Gao C, Jovasevic V, Guedea AL, Radulovic J. 2011. NMDA receptors in retrosplenial cortex are necessary for retrieval of recent and remote context fear memory. *J Neurosci* **31**:11655–11659. doi:10.1523/JNEUROSCI.2107-11.2011

Cowansage KK, Shuman T, Dillingham BC, Chang A, Golshani P, Mayford M. 2014. Direct reactivation of a coherent neocortical memory of context. *Neuron* **84**:432–441. doi:10.1016/j.neuron.2014.09.022

Crochet S, Petersen CCH. 2006. Correlating whisker behavior with membrane potential in barrel cortex of awake mice. *Nat Neurosci* **9**:608–610. doi:10.1038/nn1690

Curtis JC, Kleinfeld D. 2009. Phase-to-rate transformations encode touch in cortical neurons of a scanning sensorimotor system. *Nat Neurosci* **12**:492–501. doi:10.1038/nn.2283

Daigle TL, Madisen L, Hage TA, Valley MT, Knoblich U, Larsen RS, Takeno MM, Huang L, Gu H, Larsen R, Mills M, Bosma-Moody A, Siverts LA, Walker M, Graybuck LT, Yao Z, Fong O, Nguyen TN, Garren E, Lenz GH, Chavarha M, Pendergraft J, Harrington J, Hirokawa KE, Harris JA, Nicovich PR, McGraw MJ, Ollerenshaw DR, Smith KA, Baker CA, Ting JT, Sunkin SM, Lecoq J, Lin MZ, Boyden ES, Murphy GJ, da Costa NM, Waters J, Li L, Tasic B, Zeng H. 2018. A Suite of Transgenic Driver and Reporter Mouse Lines with Enhanced Brain-Cell-Type Targeting and Functionality. *Cell* **174**:465-480.e22. doi:10.1016/j.cell.2018.06.035

Dana H, Novak O, Guardado-Montesino M, Fransen JW, Hu A, Borghuis BG, Guo C, Kim DS, Svoboda K. 2018. Thy1 transgenic mice expressing the red fluorescent calcium indicator jRGECO1a for neuronal population imaging in vivo. *PLOS ONE* **13**:e0205444. doi:10.1371/journal.pone.0205444

Diamond ME, von Heimendahl M, Knutsen PM, Kleinfeld D, Ahissar E. 2008. “Where” and “what” in the whisker sensorimotor system. *Nat Rev Neurosci* **9**:601–612. doi:10.1038/nrn2411

Eggermann E, Kremer Y, Crochet S, Petersen CCH. 2014. Cholinergic signals in mouse barrel cortex during active whisker sensing. *Cell Rep* **9**:1654–1660. doi:10.1016/j.celrep.2014.11.005

El-Boustani S, Sermet BS, Foustoukos G, Oram TB, Yizhar O, Petersen CCH. 2020. Anatomically and functionally distinct thalamocortical inputs to primary and secondary mouse whisker somatosensory cortices. *Nat Commun* **11**:3342. doi:10.1038/s41467-020-17087-7

Esmaeili V, Tamura K, Muscinelli SP, Modirshanechi A, Boscaglia M, Lee AB, Oryshchuk A, Foustoukos G, Liu Y, Crochet S, Gerstner W, Petersen CCH. 2021. Rapid suppression and sustained activation of distinct cortical regions for a delayed sensory-triggered motor response. *Neuron* **109**:2183-2201.e9. doi:10.1016/j.neuron.2021.05.005

Feldmeyer D, Brecht M, Helmchen F, Petersen CCH, Poulet JFA, Staiger JF, Luhmann HJ, Schwarz C. 2013. Barrel cortex function. *Prog Neurobiol* **103**:3–27. doi:10.1016/j.pneurobio.2012.11.002

Finkel EA, Chang Y-T, Dasgupta R, Lubin EE, Xu D, Minamisawa G, Chang AJ, Cohen JY, O’Connor DH. 2024. Tactile processing in mouse cortex depends on action context. *Cell Reports* **43**. doi:10.1016/j.celrep.2024.113991

Franco LM, Goard MJ. 2021. A distributed circuit for associating environmental context with motor choice in retrosplenial cortex. *Science Advances* **7**:eabf9815. doi:10.1126/sciadv.abf9815

Gasselin C, Hohl B, Vernet A, Crochet S, Petersen CCH. 2021. Cell-type-specific nicotinic input disinhibits mouse barrel cortex during active sensing. *Neuron* **109**:778-787.e3. doi:10.1016/j.neuron.2020.12.018

Gershman SJ. 2017. Context-dependent learning and causal structure. *Psychon Bull Rev* **24**:557–565. doi:10.3758/s13423-016-1110-x

Gilbert CD, Li W. 2013. Top-down influences on visual processing. *Nat Rev Neurosci* **14**:350–363. doi:10.1038/nrn3476

Goldman-Rakic PS. 1995. Cellular basis of working memory. *Neuron* **14**:477–485. doi:10.1016/0896-6273(95)90304-6

Griffiths CS, Lebert JM, Sollini J, Bizley JK. 2024. Gradient boosted decision trees reveal nuances of auditory discrimination behavior. *PLOS Computational Biology* **20**:e1011985. doi:10.1371/journal.pcbi.1011985

Grinsztajn L, Oyallon E, Varoquaux G. 2022. Why do tree-based models still outperform deep learning on tabular data? doi:10.48550/arXiv.2207.08815

Guo ZV, Li N, Huber D, Ophir E, Gutnisky D, Ting JT, Feng G, Svoboda K. 2014. Flow of cortical activity underlying a tactile decision in mice. *Neuron* **81**:179–194. doi:10.1016/j.neuron.2013.10.020

Hajnal MA, Tran D, Szabó Z, Albert A, Safaryan K, Einstein M, Vallejo Martelo M, Polack P-O, Golshani P, Orbán G. 2024. Shifts in attention drive context-dependent subspace encoding in anterior cingulate cortex in mice during decision making. *Nat Commun* **15**:5559. doi:10.1038/s41467-024-49845-2

Harris JA, Hirokawa KE, Sorensen SA, Gu H, Mills M, Ng LL, Bohn P, Mortrud M, Ouellette B, Kidney J, Smith KA, Dang C, Sunkin S, Bernard A, Oh SW, Madisen L, Zeng H. 2014. Anatomical

characterization of Cre driver mice for neural circuit mapping and manipulation. *Front Neural Circuits* **8**:76. doi:10.3389/fncir.2014.00076

Harris KD. 2021. Nonsense correlations in neuroscience. doi:10.1101/2020.11.29.402719

Harris KD, Mrsic-Flogel TD. 2013. Cortical connectivity and sensory coding. *Nature* **503**:51–58. doi:10.1038/nature12654

Hasselmo ME. 2006. The role of acetylcholine in learning and memory. *Curr Opin Neurobiol* **16**:710–715. doi:10.1016/j.conb.2006.09.002

Hattori R, Komiyama T. 2022. Context-dependent persistency as a coding mechanism for robust and widely distributed value coding. *Neuron* **110**:502-515.e11. doi:10.1016/j.neuron.2021.11.001

Hippenmeyer S, Vrieseling E, Sigrist M, Portmann T, Laengle C, Ladle DR, Arber S. 2005. A developmental switch in the response of DRG neurons to ETS transcription factor signaling. *PLoS Biol* **3**:e159. doi:10.1371/journal.pbio.0030159

International Brain Laboratory, Angelaki D, Benson B, Benson J, Birman D, Bonacchi N, Bougrova K, Bruijns SA, Carandini M, Catarino JA, Chapuis GA, Churchland AK, Dan Y, Davatolhagh F, Dayan P, DeWitt EE, Engel TA, Fabbri M, Faulkner M, Fiete IR, Findling C, Freitas-Silva L, Gerçek B, Harris KD, Häusser M, Hofer SB, Hu F, Hubert F, Huntenburg JM, Khanal A, Krasniak CS, Langdon C, Langfield C, Lau PYP, Mainen ZF, Meijer GT, Miska NJ, Mrsic-Flogel TD, Noel J-P, Nylund K, Pan-Vazquez A, Paninski L, Pouget A, Rossant C, Roth N, Schaeffer R, Schartner M, Shi Y, Socha KZ, Steinmetz NA, Svoboda K, Urai AE, Wells MJ, West SJ, Whiteway MR, Winter O, Witten IB. 2025. A brain-wide map of neural activity during complex behaviour. *Nature* **645**:177–191. doi:10.1038/s41586-025-09235-0

Keene CS, Bucci DJ. 2008. Involvement of the retrosplenial cortex in processing multiple conditioned stimuli. *Behav Neurosci* **122**:651–658. doi:10.1037/0735-7044.122.3.651

Khilkevich A, Lohse M, Low R, Orsolic I, Bozic T, Windmill P, Mrsic-Flogel TD. 2024. Brain-wide dynamics linking sensation to action during decision-making. *Nature*. doi:10.1038/s41586-024-07908-w

Kim J-H, Ma D-H, Jung E, Choi I, Lee S-H. 2021. Gated feedforward inhibition in the frontal cortex releases goal-directed action. *Nat Neurosci* **24**:1452–1464. doi:10.1038/s41593-021-00910-9

Kira S, Safaai H, Morcos AS, Panzeri S, Harvey CD. 2023. A distributed and efficient population code of mixed selectivity neurons for flexible navigation decisions. *Nat Commun* **14**:2121. doi:10.1038/s41467-023-37804-2

Kleinfeld D, Deschênes M. 2011. Neuronal basis for object location in the vibrissa scanning sensorimotor system. *Neuron* **72**:455–468. doi:10.1016/j.neuron.2011.10.009

Klein-Flügge MC, Bongioanni A, Rushworth MFS. 2022. Medial and orbital frontal cortex in decision-making and flexible behavior. *Neuron* **110**:2743–2770. doi:10.1016/j.neuron.2022.05.022

Kuchibhotla KV, Gill JV, Lindsay GW, Papadoyannis ES, Field RE, Sten TAH, Miller KD, Froemke RC. 2017. Parallel processing by cortical inhibition enables context-dependent behavior. *Nat Neurosci* **20**:62–71. doi:10.1038/nn.4436

Kwon SE, Yang H, Minamisawa G, O'Connor DH. 2016. Sensory and decision-related activity propagate in a cortical feedback loop during touch perception. *Nat Neurosci* **19**:1243–1249. doi:10.1038/nn.4356

Le Merre P, Esmaeili V, Charrière E, Galan K, Salin P-A, Petersen CCH, Crochet S. 2018. Reward-based learning drives rapid sensory signals in medial prefrontal cortex and dorsal hippocampus necessary for goal-directed behavior. *Neuron* **97**:83-91.e5. doi:10.1016/j.neuron.2017.11.031

Li Y, Ren M, Liu B, Jiang T, Jia X, Zhang H, Gong H, Wang X. 2025. Dissection of the long-range circuit of the mouse intermediate retrosplenial cortex. *Commun Biol* **8**:56. doi:10.1038/s42003-025-07463-8

Liu D, Gu X, Zhu J, Zhang X, Han Z, Yan W, Cheng Q, Hao J, Fan H, Hou R, Chen Z, Chen Y, Li CT. 2014. Medial prefrontal activity during delay period contributes to learning of a working memory task. *Science* **346**:458–463. doi:10.1126/science.1256573

1068 Liu Y, Bech P, Tamura K, Délez LT, Crochet S, Petersen CCH. 2024. Cell class-specific long-range axonal
1069 projections of neurons in mouse whisker-related somatosensory cortices. *eLife* **13**:RP97602.
1070 doi:10.7554/eLife.97602
1071 Lohani S, Moberly AH, Benisty H, Landa B, Jing M, Li Y, Higley MJ, Cardin JA. 2022. Spatiotemporally
1072 heterogeneous coordination of cholinergic and neocortical activity. *Nat Neurosci* **25**:1706–
1073 1713. doi:10.1038/s41593-022-01202-6
1074 Lundberg S, Lee S-I. 2017. A Unified Approach to Interpreting Model Predictions.
1075 doi:10.48550/arXiv.1705.07874
1076 Madisen L, Zwingman TA, Sunkin SM, Oh SW, Zariwala HA, Gu H, Ng LL, Palmiter RD, Hawrylycz MJ,
1077 Jones AR, Lein ES, Zeng H. 2010. A robust and high-throughput Cre reporting and
1078 characterization system for the whole mouse brain. *Nat Neurosci* **13**:133–140.
1079 doi:10.1038/nn.2467
1080 Mahn M, Gibor L, Patil P, Cohen-Kashi Malina K, Oring S, Printz Y, Levy R, Lampl I, Yizhar O. 2018.
1081 High-efficiency optogenetic silencing with soma-targeted anion-conducting
1082 channelrhodopsins. *Nat Commun* **9**:4125. doi:10.1038/s41467-018-06511-8
1083 Mao D, Kandler S, McNaughton BL, Bonin V. 2017. Sparse orthogonal population representation of
1084 spatial context in the retrosplenial cortex. *Nat Commun* **8**:243. doi:10.1038/s41467-017-
1085 00180-9
1086 Mao D, Neumann AR, Sun J, Bonin V, Mohajerani MH, McNaughton BL. 2018. Hippocampus-
1087 dependent emergence of spatial sequence coding in retrosplenial cortex. *Proceedings of the*
1088 *National Academy of Sciences* **115**:8015–8018. doi:10.1073/pnas.1803224115
1089 Marton TF, Seifikar H, Luongo FJ, Lee AT, Sohal VS. 2018. Roles of Prefrontal Cortex and Mediodorsal
1090 Thalamus in Task Engagement and Behavioral Flexibility. *J Neurosci* **38**:2569–2578.
1091 doi:10.1523/JNEUROSCI.1728-17.2018
1092 Mathis A, Mamidanna P, Cury KM, Abe T, Murthy VN, Mathis MW, Bethge M. 2018. DeepLabCut:
1093 markerless pose estimation of user-defined body parts with deep learning. *Nat Neurosci*
1094 **21**:1281–1289. doi:10.1038/s41593-018-0209-y
1095 Mayrhofer JM, El-Boustani S, Foustoukos G, Auffret M, Tamura K, Petersen CCH. 2019. Distinct
1096 contributions of whisker sensory cortex and tongue-jaw motor cortex in a goal-directed
1097 sensorimotor transformation. *Neuron* **103**:1034-1043.e5. doi:10.1016/j.neuron.2019.07.008
1098 McGinley MJ, David SV, McCormick DA. 2015. Cortical Membrane Potential Signature of Optimal
1099 States for Sensory Signal Detection. *Neuron* **87**:179–192. doi:10.1016/j.neuron.2015.05.038
1100 Miyashita T, Feldman DE. 2013. Behavioral detection of passive whisker stimuli requires
1101 somatosensory cortex. *Cereb Cortex* **23**:1655–1662. doi:10.1093/cercor/bhs155
1102 Mukherjee A, Lam NH, Wimmer RD, Halassa MM. 2021. Thalamic circuits for independent control of
1103 prefrontal signal and noise. *Nature* **600**:100–104. doi:10.1038/s41586-021-04056-3
1104 Musall S, Kaufman MT, Juavinett AL, Gluf S, Churchland AK. 2019. Single-trial neural dynamics are
1105 dominated by richly varied movements. *Nat Neurosci* **22**:1677–1686. doi:10.1038/s41593-
1106 019-0502-4
1107 O'Connor DH, Peron SP, Huber D, Svoboda K. 2010. Neural activity in barrel cortex underlying
1108 vibrissa-based object localization in mice. *Neuron* **67**:1048–1061.
1109 doi:10.1016/j.neuron.2010.08.026
1110 Oh SW, Harris JA, Ng L, Winslow B, Cain N, Mihalas S, Wang Q, Lau C, Kuan L, Henry AM, Mortrud MT,
1111 Ouellette B, Nguyen TN, Sorensen SA, Slaughterbeck CR, Wakeman W, Li Y, Feng D, Ho A,
1112 Nicholas E, Hirokawa KE, Bohn P, Joines KM, Peng H, Hawrylycz MJ, Phillips JW, Hohmann JG,
1113 Wohnoutka P, Gerfen CR, Koch C, Bernard A, Dang C, Jones AR, Zeng H. 2014. A mesoscale
1114 connectome of the mouse brain. *Nature* **508**:207–214. doi:10.1038/nature13186
1115 Ortiz AV, Aziz D, Hestrin S. 2020. Motivation and engagement during visually guided behavior. *Cell*
1116 *Rep* **33**:108272. doi:10.1016/j.celrep.2020.108272
1117 Oryshchuk A, Sourmpis C, Weverbergh J, Asri R, Esmaeili V, Modirshanechi A, Gerstner W, Petersen
1118 CCH, Crochet S. 2024. Distributed and specific encoding of sensory, motor, and decision

information in the mouse neocortex during goal-directed behavior. *Cell Rep* **43**:113618. doi:10.1016/j.celrep.2023.113618

Pedregosa F, Varoquaux G, Gramfort A, Michel V, Thirion B, Grisel O, Blondel M, Prettenhofer P, Weiss R, Dubourg V, Vanderplas J, Passos A, Cournapeau D, Brucher M, Perrot M, Duchesnay E. 2011. Scikit-learn: Machine Learning in Python. *Journal of Machine Learning Research* **12**:2825–2830.

Petersen CCH. 2019. Sensorimotor processing in the rodent barrel cortex. *Nat Rev Neurosci* **20**:533–546. doi:10.1038/s41583-019-0200-y

Place R, Farovik A, Brockmann M, Eichenbaum H. 2016. Bidirectional prefrontal-hippocampal interactions support context-guided memory. *Nat Neurosci* **19**:992–994. doi:10.1038/nn.4327

Poort J, Wilmes KA, Blot A, Chadwick A, Sahani M, Clopath C, Mrsic-Flogel TD, Hofer SB, Khan AG. 2022. Learning and attention increase visual response selectivity through distinct mechanisms. *Neuron* **110**:686-697.e6. doi:10.1016/j.neuron.2021.11.016

Poulet JFA, Fernandez LMJ, Crochet S, Petersen CCH. 2012. Thalamic control of cortical states. *Nat Neurosci* **15**:370–372. doi:10.1038/nn.3035

Poulet JFA, Petersen CCH. 2008. Internal brain state regulates membrane potential synchrony in barrel cortex of behaving mice. *Nature* **454**:881–885. doi:10.1038/nature07150

Reimer J, Froudarakis E, Cadwell CR, Yatsenko D, Denfield GH, Tolias AS. 2014. Pupil Fluctuations Track Fast Switching of Cortical States during Quiet Wakefulness. *Neuron* **84**:355–362. doi:10.1016/j.neuron.2014.09.033

Resulaj A, Ruediger S, Olsen SR, Scanziani M. 2018. First spikes in visual cortex enable perceptual discrimination. *Elife* **7**. doi:10.7554/eLife.34044

Robinson S, Poorman CE, Marder TJ, Bucci DJ. 2012. Identification of Functional Circuitry between Retrosplenial and Postrhinal Cortices during Fear Conditioning. *J Neurosci* **32**:12076–12086. doi:10.1523/JNEUROSCI.2814-12.2012

Romo R, Brody CD, Hernández A, Lemus L. 1999. Neuronal correlates of parametric working memory in the prefrontal cortex. *Nature* **399**:470–473. doi:10.1038/20939

Rossi-Pool R, Zainos A, Alvarez M, Diaz-deLeon G, Romo R. 2021. A continuum of invariant sensory and behavioral-context perceptual coding in secondary somatosensory cortex. *Nat Commun* **12**:2000. doi:10.1038/s41467-021-22321-x

Rübel O, Tritt A, Ly R, Dichter BK, Ghosh S, Niu L, Baker P, Soltesz I, Ng L, Svoboda K, Frank L, Bouchard KE. 2022. The Neurodata Without Borders ecosystem for neurophysiological data science. *eLife* **11**:e78362. doi:10.7554/eLife.78362

Saalmann YB, Pinsk MA, Wang L, Li X, Kastner S. 2012. The Pulvinar Regulates Information Transmission Between Cortical Areas Based on Attention Demands. *Science* **337**:753–756. doi:10.1126/science.1223082

Sachidhanandam S, Sreenivasan V, Kyriakatos A, Kremer Y, Petersen CCH. 2013. Membrane potential correlates of sensory perception in mouse barrel cortex. *Nat Neurosci* **16**:1671–1677. doi:10.1038/nn.3532

Schoenbaum G, Roesch MR, Stalnaker TA, Takahashi YK. 2009. A new perspective on the role of the orbitofrontal cortex in adaptive behaviour. *Nat Rev Neurosci* **10**:885–892. doi:10.1038/nrn2753

Shahsavarani S, Thibodeaux DN, Xu W, Kim SH, Lodgher F, Nwokeabia C, Cambareri M, Yagielski AJ, Zhao HT, Handwerker DA, Gonzalez-Castillo J, Bandettini PA, Hillman EMC. 2023. Cortex-wide neural dynamics predict behavioral states and provide a neural basis for resting-state dynamic functional connectivity. *Cell Reports* **42**:112527. doi:10.1016/j.celrep.2023.112527

Siegle JH, Jia X, Durand S, Gale S, Bennett C, Graddis N, Heller G, Ramirez TK, Choi H, Luviano JA, Groblewski PA, Ahmed R, Arkhipov A, Bernard A, Billeh YN, Brown D, Buice MA, Cain N, Caldejon S, Casal L, Cho A, Chvilicek M, Cox TC, Dai K, Denman DJ, de Vries SEJ, Dietzman R, Esposito L, Farrell C, Feng D, Galbraith J, Garrett M, Gelfand EC, Hancock N, Harris JA, Howard R, Hu B, Hytnen R, Iyer R, Jessett E, Johnson K, Kato I, Kiggins J, Lambert S, Lecoq J,

Ledochowitsch P, Lee JH, Leon A, Li Y, Liang E, Long F, Mace K, Melchior J, Millman D, Mollenkopf T, Nayan C, Ng L, Ngo K, Nguyen T, Nicovich PR, North K, Ocker GK, Ollerenshaw D, Oliver M, Pachitariu M, Perkins J, Reding M, Reid D, Robertson M, Ronellenfitch K, Seid S, Slaughterbeck C, Stoecklin M, Sullivan D, Sutton B, Swapp J, Thompson C, Turner K, Wakeman W, Whitesell JD, Williams D, Williford A, Young R, Zeng H, Naylor S, Phillips JW, Reid RC, Mihalas S, Olsen SR, Koch C. 2021. Survey of spiking in the mouse visual system reveals functional hierarchy. *Nature* **592**:86–92. doi:10.1038/s41586-020-03171-x

Sippy T, Lapray D, Crochet S, Petersen CCH. 2015. Cell-type-specific sensorimotor processing in striatal projection neurons during goal-directed behavior. *Neuron* **88**:298–305. doi:10.1016/j.neuron.2015.08.039

Sit KK, Goard MJ. 2023. Coregistration of heading to visual cues in retrosplenial cortex. *Nat Commun* **14**:1992. doi:10.1038/s41467-023-37704-5

Staiger JF, Petersen CCH. 2021. Neuronal circuits in barrel cortex for whisker sensory perception. *Physiol Rev* **101**:353–415. doi:10.1152/physrev.00019.2019

Stern CE, Sherman SJ, Kirchhoff BA, Hasselmo ME. 2001. Medial temporal and prefrontal contributions to working memory tasks with novel and familiar stimuli. *Hippocampus* **11**:337–346. doi:10.1002/hipo.1048

Sugar J, Witter MP, van Strien NM, Cappaert NLM. 2011. The retrosplenial cortex: intrinsic connectivity and connections with the (para)hippocampal region in the rat. An interactive connectome. *Front Neuroinform* **5**:7. doi:10.3389/fninf.2011.00007

Sun W, Choi I, Stoyanov S, Senkov O, Ponimaskin E, Winter Y, Pakan JMP, Dityatev A. 2021. Context value updating and multidimensional neuronal encoding in the retrosplenial cortex. *Nat Commun* **12**:6045. doi:10.1038/s41467-021-26301-z

Takahashi N, Ebner C, Sigl-Glöckner J, Moberg S, Nierwetberg S, Larkum ME. 2020. Active dendritic currents gate descending cortical outputs in perception. *Nat Neurosci* **23**:1277–1285. doi:10.1038/s41593-020-0677-8

Tamamaki N, Yanagawa Y, Tomioka R, Miyazaki J-I, Obata K, Kaneko T. 2003. Green fluorescent protein expression and colocalization with calretinin, parvalbumin, and somatostatin in the GAD67-GFP knock-in mouse. *J Comp Neurol* **467**:60–79. doi:10.1002/cne.10905

Tamura K, Bech P, Mizuno H, Veaute L, Crochet S, Petersen CCH. 2025. Cell-class-specific orofacial motor maps in mouse neocortex. *Current Biology* **35**:1382-1390.e5. doi:10.1016/j.cub.2025.01.056

Todd TP, Fournier DI, Bucci DJ. 2019. Retrosplenial cortex and its role in cue-specific learning and memory. *Neuroscience & Biobehavioral Reviews* **107**:713–728. doi:10.1016/j.neubiorev.2019.04.016

Tovote P, Fadok JP, Lüthi A. 2015. Neuronal circuits for fear and anxiety. *Nat Rev Neurosci* **16**:317–331. doi:10.1038/nrn3945

Urbain N, Salin PA, Libourel P-A, Comte J-C, Gentet LJ, Petersen CCH. 2015. Whisking-Related Changes in Neuronal Firing and Membrane Potential Dynamics in the Somatosensory Thalamus of Awake Mice. *Cell Rep* **13**:647–656. doi:10.1016/j.celrep.2015.09.029

Vedder LC, Miller AMP, Harrison MB, Smith DM. 2017. Retrosplenial Cortical Neurons Encode Navigational Cues, Trajectories and Reward Locations During Goal Directed Navigation. *Cereb Cortex* **27**:3713–3723. doi:10.1093/cercor/bhw192

Wietek J, Nozownik A, Pulin M, Saraf-Sinik I, Matosevich N, Gowrishankar R, Gat A, Malan D, Brown BJ, Dine J, Imambocus BN, Levy R, Sauter K, Litvin A, Regev N, Subramaniam S, Abrera K, Summarli D, Goren EM, Mizrachi G, Bitton E, Benjamin A, Copits BA, Sasse P, Rost BR, Schmitz D, Bruchas MR, Soba P, Oren-Suissa M, Nir Y, Wiegert JS, Yizhar O. 2024. A bistable inhibitory optoGPCR for multiplexed optogenetic control of neural circuits. *Nat Methods* 1–13. doi:10.1038/s41592-024-02285-8

Wu Z, Litwin-Kumar A, Shamash P, Taylor A, Axel R, Shadlen MN. 2020. Context-dependent decision making in a premotor circuit. *Neuron* **106**:316-328.e6. doi:10.1016/j.neuron.2020.01.034

1222 Yamashita T, Petersen CCH. 2016. Target-specific membrane potential dynamics of neocortical
1223 projection neurons during goal-directed behavior. *eLife* **5**:15798. doi:10.7554/eLife.15798
1224 Yamawaki N, Radulovic J, Shepherd GMG. 2016. A Corticocortical Circuit Directly Links Retrosplenial
1225 Cortex to M2 in the Mouse. *J Neurosci* **36**:9365–9374. doi:10.1523/JNEUROSCI.1099-16.2016
1226 Yang H, Kwon SE, Severson KS, O'Connor DH. 2016. Origins of choice-related activity in mouse
1227 somatosensory cortex. *Nat Neurosci* **19**:127–134. doi:10.1038/nn.4183
1228 Zhao S, Ting JT, Atallah HE, Qiu L, Tan J, Gloss B, Augustine GJ, Deisseroth K, Luo M, Graybiel AM,
1229 Feng G. 2011. Cell type–specific channelrhodopsin-2 transgenic mice for optogenetic
1230 dissection of neural circuitry function. *Nat Methods* **8**:745–752. doi:10.1038/nmeth.1668
1231 Zhou H, Schafer RJ, Desimone R. 2016. Pulvinar-Cortex Interactions in Vision and Attention. *Neuron*
1232 **89**:209–220. doi:10.1016/j.neuron.2015.11.034
1233

Figure 1

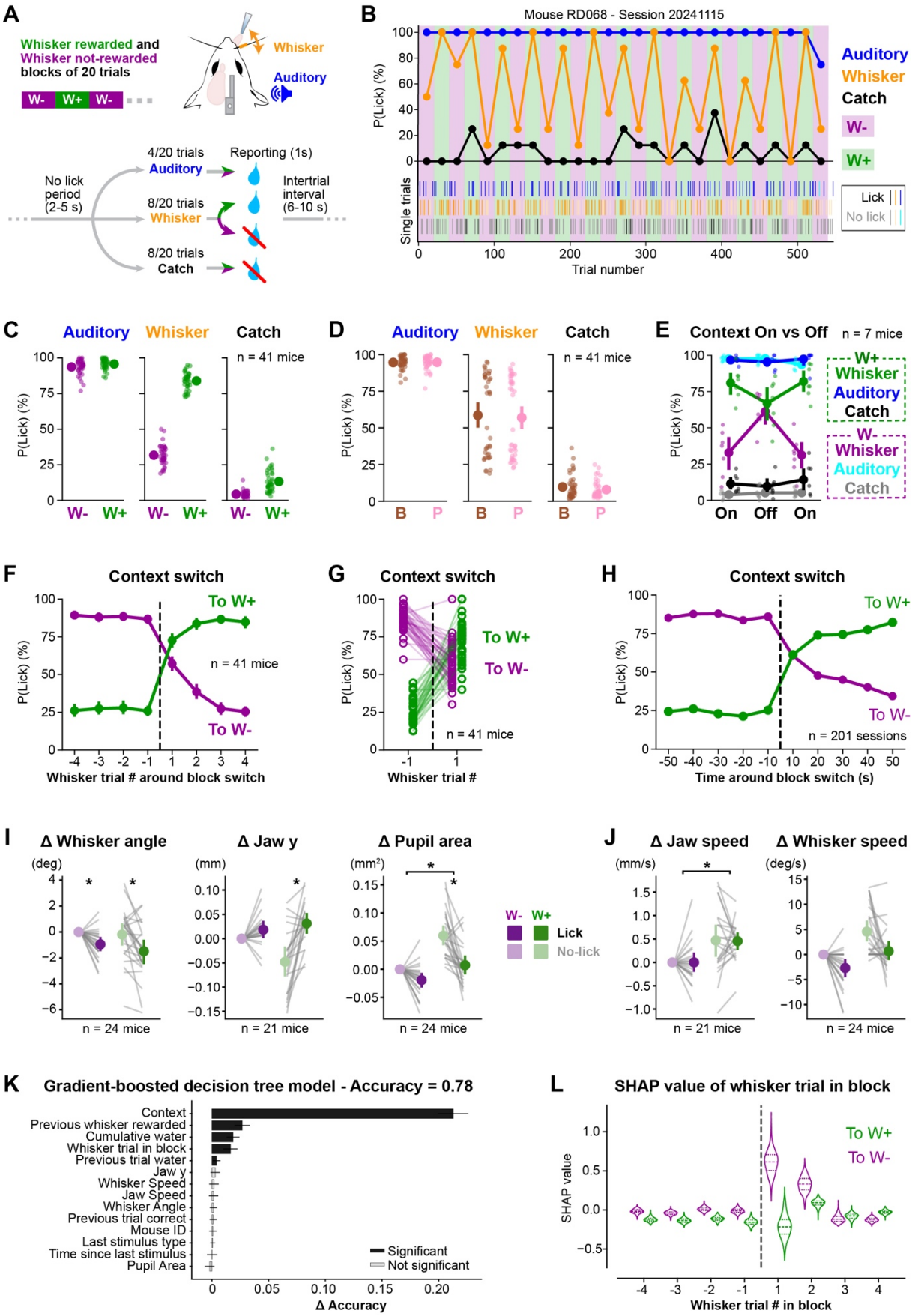
A
Whisker rewarded and
Whisker not-rewarded
blocks of 20 trials
W- W+ W-
Whisker
Auditory
No lick
period
(2-5 s)
4/20 trials
Auditory
8/20 trials
Whisker
8/20 trials
Catch
Reporting (1s)
Intertrial
interval
(6-10 s)
B
Mouse RD068 - Session 20241115
P(Lick) (%)
Single trials
Trial number
Auditory
Whisker
Catch
W-
W+
Lick
No lick
C
Auditory
Whisker
Catch
n = 41 mice
P(Lick) (%)
W- W+
D
Auditory
Whisker
Catch
n = 41 mice
B P
E
Context On vs Off
n = 7 mice
W+
Whisker
Auditory
Catch
W-
Whisker
Auditory
Catch
On Off On
F
Context switch
To W+
To W-
n = 41 mice
Whisker trial # around block switch
G
Context switch
To W+
To W-
n = 41 mice
Whisker trial #
H
Context switch
To W+
To W-
n = 201 sessions
Time around block switch (s)
I
Δ Whisker angle
(deg)
n = 24 mice
Δ Jaw y
(mm)
n = 21 mice
Δ Pupil area
(mm²)
n = 24 mice
W- W+
Lick
No-lick
J
Δ Jaw speed
(mm/s)
n = 21 mice
Δ Whisker speed
(deg/s)
n = 24 mice
K
Gradient-boosted decision tree model - Accuracy = 0.78
Context
Previous whisker rewarded
Cumulative water
Whisker trial in block
Previous trial water
Jaw y
Whisker Speed
Jaw Speed
Whisker Angle
Previous trial correct
Mouse ID
Last stimulus type
Time since last stimulus
Pupil Area
Significant
Not significant
Δ Accuracy
L
SHAP value of whisker trial in block
SHAP value
To W+
To W-
Whisker trial # in block

Figure 1. A context-dependent whisker detection task. (**A**) Schematic of the task structure. (**B**) Block-average lick rate in one example expert session for whisker trials (orange), auditory trials (blue) and catch trials (black). W+ and W- blocks are shown by green and purple shaded areas, respectively. Single trials are shown by individual ticks (below). (**C**) Averaged lick probability for whisker, auditory and catch trials in W+ and W- context. Small dots represent individual mice (n = 41 mice, 201 sessions); large-filled circles represent grand-averages with error bars showing the 95% confidence interval. (**D**) Same as C, but split according to brown (B) or pink (P) noise context identity. (**E**) As a control, the contextual brown and pink noises (Context On) were replaced by constant white noise (Context Off) for one session (n = 7 mice). (**F**) Averaged lick probability for whisker trials centered on context transitions. From W- to W+ in green and from W+ to W- in purple (n = 41 mice). (**G**) Lick probability at last and first whisker trials around context transition (n = 41 mice). (**H**) Lick probability in response to the last and first whisker trial around context transition according to the delay at which it occurs. Transition from W- to W+ in green and from W+ to W- in magenta. (**I&J**) Quantification of orofacial posture (panel I) and movements (panel J) during the no-lick window preceding trial onset. Each line represents an individual mouse; large-filled circles represent grand-averages with error bars showing the 95% confidence interval. (**K**) Drop in accuracy for permutation of labels for each of the parameters of the gradient-boosted model predicting single-trial responses. (**L**) SHAP values for the 'whisker trial in block' parameter aligned on context transition from W+ to W- in magenta and from W- to W+ in green.

Figure 2

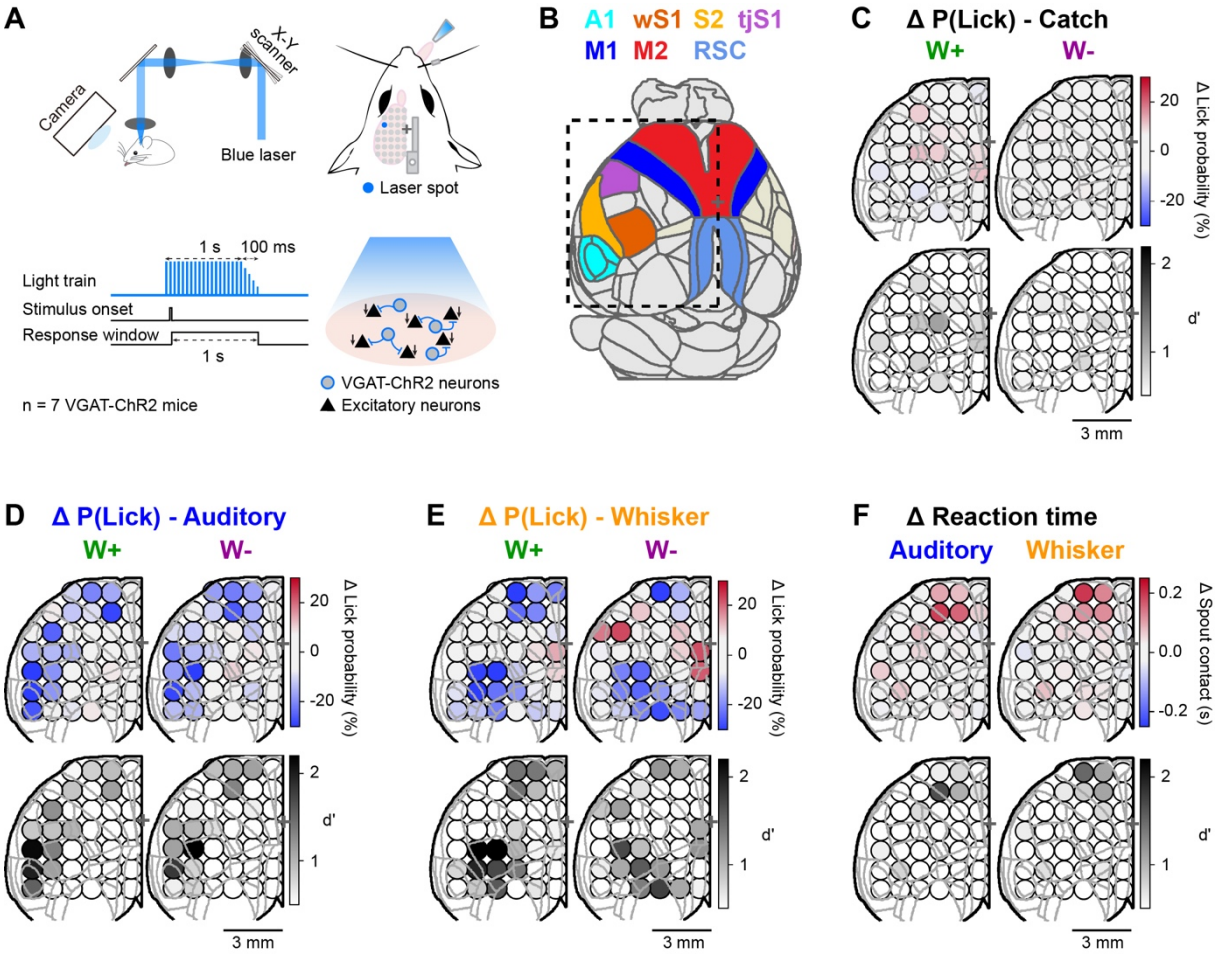

Figure 2. Optogenetic inactivation screen. (**A**) Schematic of the optoinhibition screening in VGAT-ChR2 mice. (**B**) 30° rotated top view of the Allen mouse brain atlas, as in the experimental setup. (**C**) Top: Grid map showing changes in lick probability, ΔP(Lick), during catch trials in W- and W+ evoked by optogenetic inactivation of the target area. Bottom: d' computed between the distribution of ΔP(Lick) in stim trials and a null distribution computed by shuffling all trials 1,000 times. (**D**) Same as C, but for auditory trials. (**E**) Same as C, but for whisker trials. (**F**) Top: Grid map showing change in lick reaction time (tongue-spout contact time) in correct response to auditory and whisker trials during optogenetic inactivation of the target area relative to control trials. Bottom: associated d'.

Figure 3

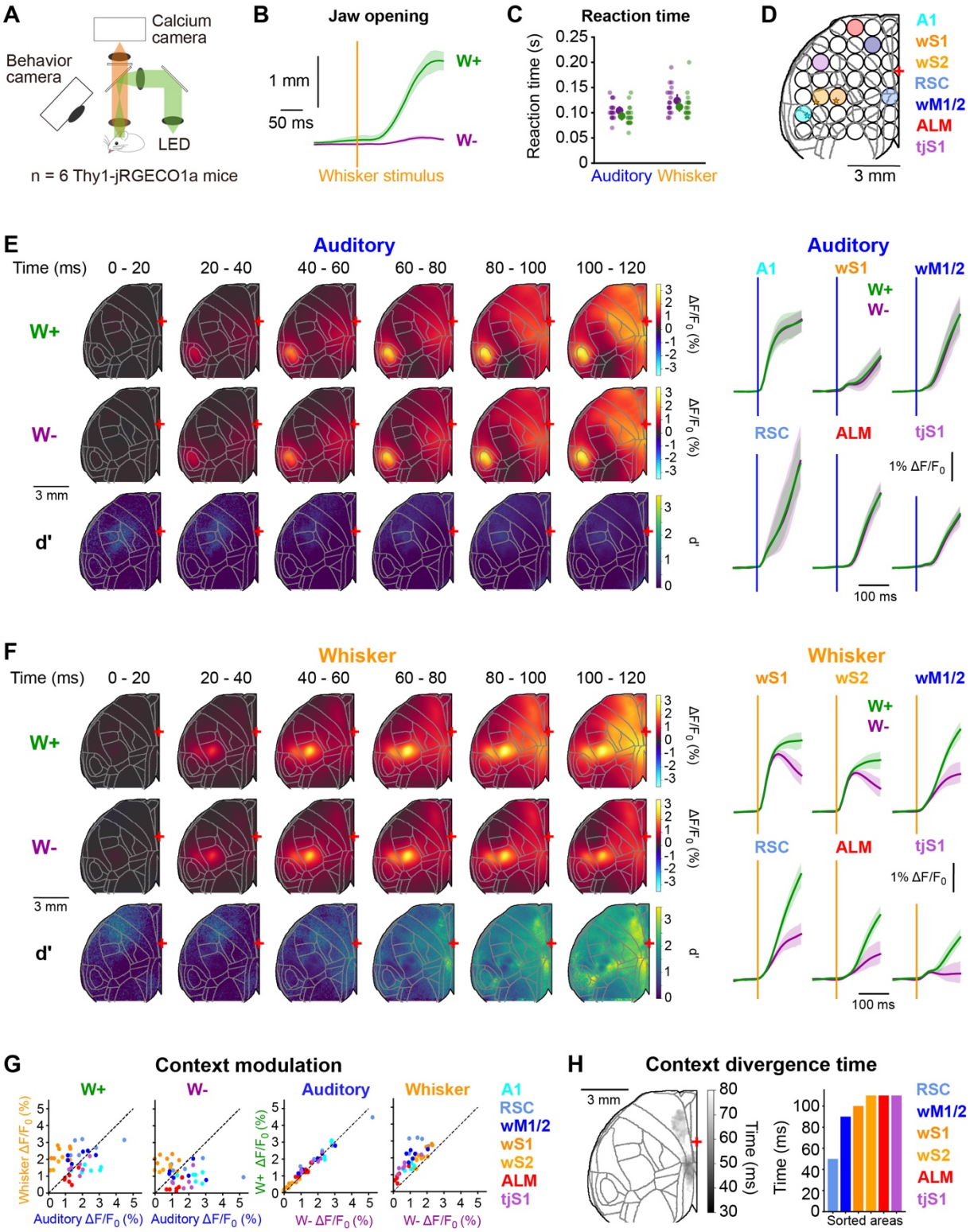
A
Calcium camera
Behavior camera
LED
n = 6 Thy1-jRGECO1a mice
B
Jaw opening
1 mm
50 ms
W+
W-
Whisker stimulus
C
Reaction time
Reaction time (s)
Auditory Whisker
D
A1
wS1
wS2
RSC
wM1/2
ALM
tjS1
3 mm
E
Auditory
Time (ms)
0 - 20
20 - 40
40 - 60
60 - 80
80 - 100
100 - 120
W+
W-
d'
ΔF/F0 (%)
3 mm
1% ΔF/F0
100 ms
F
Whisker
G
Context modulation
Auditory
Whisker
Whisker ΔF/F0 (%)
Auditory ΔF/F0 (%)
W+ ΔF/F0 (%)
W- ΔF/F0 (%)
H
Context divergence time
Time (ms)
Sorted areas

1272 **Figure 3.** Imaging cortical spatiotemporal dynamics of context-dependent
1273 sensorimotor processing. (**A**) Experimental apparatus. (**B**) Averaged time course of
1274 jaw opening aligned on whisker stimulus for correct trials in W+ (green) and W- (purple)
1275 contexts. (**C**) Reaction time in auditory and whisker trials in W- and W+ context derived
1276 from the time course of the jaw opening. (**D**) Grid map showing the target areas that
1277 are used as ROIs for trial averaged activity. The stars represent the center of mass of
1278 manually drawn ROIs centered on the peak of sensory-evoked activity for each mouse.
1279 (**E**) Left: Image series showing evolution of cortical dynamics following auditory trials
1280 in W+ (first row), in W- (second row), and d' showing time-by-time distance between
1281 W- and W+ activity maps (third row). Right: Average time-course of stimulus-evoked
1282 activity in correct auditory trials in W+ (green) and W- (magenta) of selected target
1283 areas. (**F**) Same as in E, but for whisker trials. (**G**) Left: correlation between peak $\Delta F/F_0$
1284 response to whisker and auditory trials in W+ and W-. Right: correlation between peak
1285 $\Delta F/F_0$ responses in W- and W+ for whisker and auditory trials. Each dot represents a
1286 mouse, dashed dark line represents equality of the two variables. (**H**) Left: Heatmap
1287 showing the first time at which the d' comparing W- and W+ in correct whisker passed
1288 above 2 for each pixel. Right: Same comparison, but derived from ROI time-courses
1289 shown in F.

Figure 4

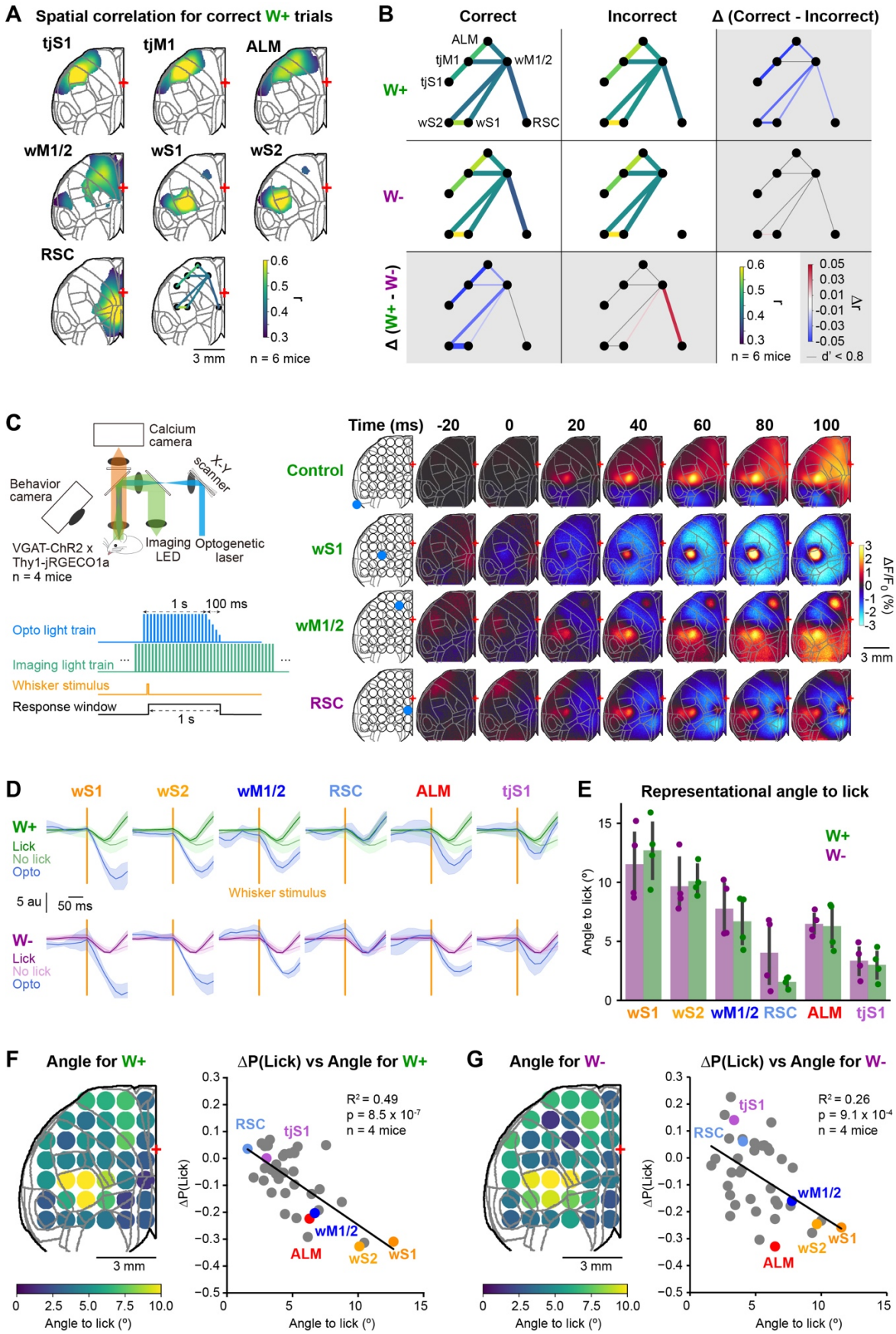
A
Spatial correlation for correct W+ trials
tjS1
tjM1
ALM
wM1/2
wS1
wS2
RSC
0.6
0.5
0.4
0.3
r
3 mm
n = 6 mice
B
Correct
Incorrect
Δ (Correct - Incorrect)
W+
W-
Δ (W+ - W-)
ALM
tjM1
wM1/2
tjS1
wS2
wS1
RSC
0.05
0.03
0.01
-0.01
-0.03
-0.05
Δr
d' < 0.8
C
Calcium camera
X-Y scanner
Behavior camera
VGAT-ChR2 x Thy1-jRGECO1a
n = 4 mice
Imaging LED
Optogenetic laser
1 s
100 ms
Opto light train
Imaging light train
Whisker stimulus
Response window
Time (ms)
-20
0
20
40
60
80
100
Control
wS1
wM1/2
RSC
ΔF/F0 (%)
3 mm
D
wS1
wS2
wM1/2
RSC
ALM
tjS1
W+
Lick
No lick
Opto
Whisker stimulus
5 au
50 ms
W-
Lick
No lick
Opto
E
Representational angle to lick
W+
W-
Angle to lick (°)
wS1
wS2
wM1/2
RSC
ALM
tjS1
F
Angle for W+
3 mm
Angle to lick (°)
ΔP(Lick) vs Angle for W+
R² = 0.49
p = 8.5 x 10⁻⁷
n = 4 mice
RSC
tjS1
wM1/2
ALM
wS2
wS1
ΔP(Lick)
Angle to lick (°)
G
Angle for W-
3 mm
Angle to lick (°)
ΔP(Lick) vs Angle for W-
R² = 0.26
p = 9.1 x 10⁻⁴
n = 4 mice
tjS1
RSC
wM1/2
wS2
wS1
ALM
ΔP(Lick)
Angle to lick (°)

1292 **Figure 4.** Context-dependent interactions across cortical areas. (**A**) Map of correlation
1293 values for pixels significantly correlated to each seed. (**B**) Graph of connected network
1294 for correct and incorrect trials in W- and W+ extracted from maps of significant pixel to
1295 seed correlation. The rightmost column shows the difference between correct and
1296 incorrect trials in both contexts. The bottom row shows the difference between W+ and
1297 W- for correct and incorrect trials. (**C**) Left: schematic of the experimental setup for
1298 simultaneous optogenetic and imaging. Right: averaged image series for whisker trials
1299 in W+ contexts for control trials and 3 example inhibition locations. Time of frames in
1300 ms is aligned to whisker onset, and the optogenetic train starts in the immediately prior
1301 inter-frame interval. (**D**) Time course of activity projected on PC3 for whisker trials with
1302 optogenetic inhibition in W+ and W-. Dark green lines show whisker trials with lick in
1303 W+ for control trials, whereas light green lines show the same for no–lick outcome.
1304 Dark purple and light purple lines show the equivalent in W-. Blue lines show the
1305 projected activity for optogenetic inhibition of each of the selected grid locations in W+
1306 and W-. Shaded areas represent 95% confidence intervals. (**E**) Quantification of the
1307 angle in PC3 between the optogenetic low dimensional projection and control-lick
1308 projection. Each dot represents a mouse and error bars are 95% confidence intervals.
1309 (**F**) Left: Grid projection of the average angle for each mouse between projections after
1310 optogenetic stimulation and control-lick projection in W+. Right: Pearson correlation
1311 between the angle in the average map (see left panel) and changes in lick probability
1312 for the opto-widefield mice in W+. (**G**) Same as F, but for W-.

Retrosplenial cortex enables context-dependent goal-directed sensorimotor transformation

Pol Bech, Robin Dard, Jules Lebert, Lana Smith, Axel Bisi,
Anthony Renard, Sylvain Crochet, and Carl Petersen

Supplemental information consists of four supplemental figures:

Figure 1 – figure supplement 1
Figure 2 – figure supplement 1
Figure 3 – figure supplement 1
Figure 4 – figure supplement 1

Figure 1 – figure supplement 1

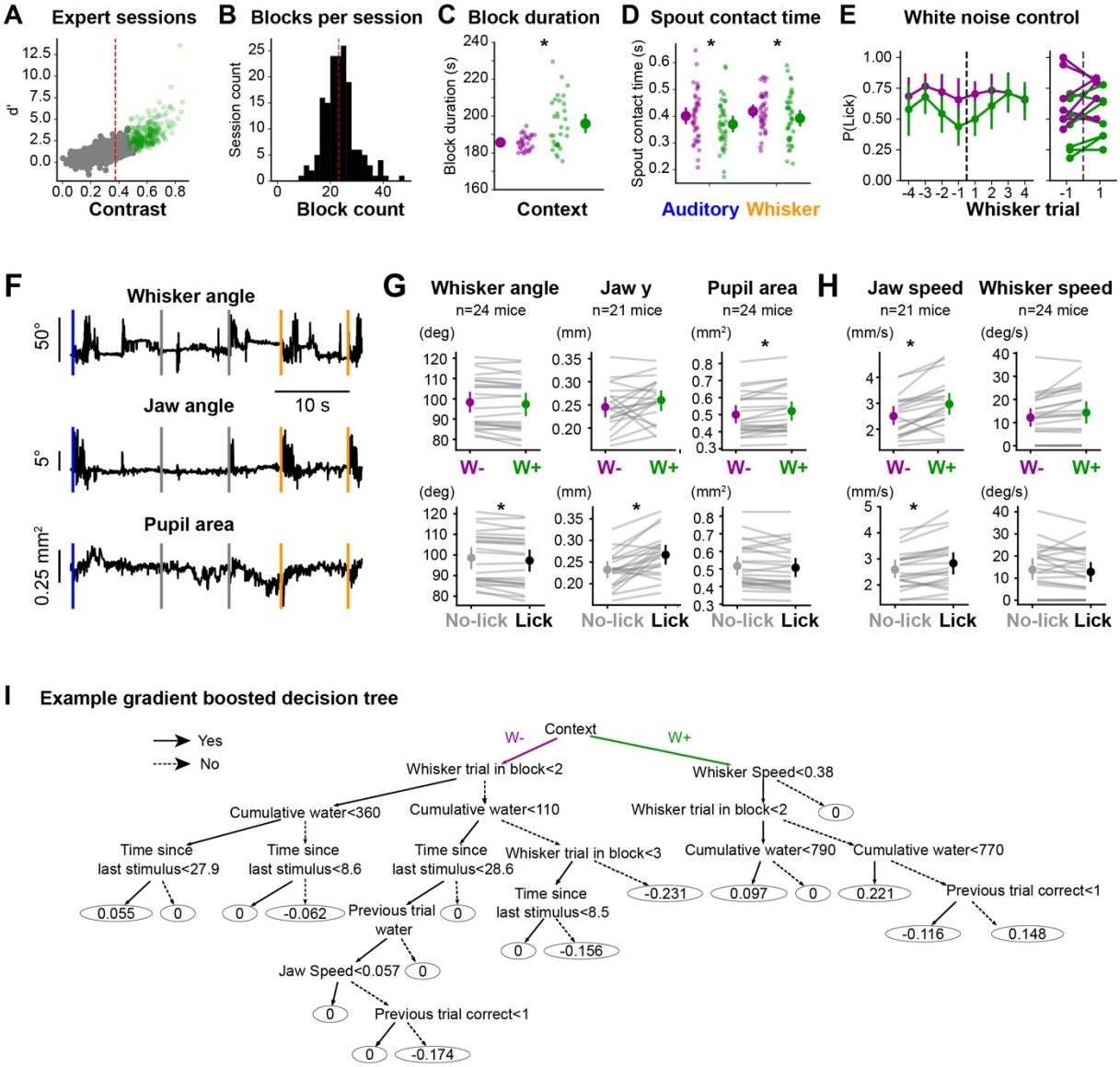

Figure 1 – figure supplement 1. (**A**) Correlation between contrast value used for selection of expert sessions and discriminability index d'. Each dot represents a session. The dashed red line represents the threshold for the selection of expert sessions. Sessions with significantly above threshold average contrast values were classified as expert and shown in green. (**B**) Histogram showing the distribution of the total number of blocks in expert sessions. The dashed red line represents the average of the distribution. (**C**) Average duration of single context block. Each dot represents a mouse. Context block durations were averaged within session then further average across sessions to preserved paired data for each mouse. Population average is shown with the 95% confidence interval of the mean. Whisker rewarded context blocks were significantly longer than whisker non-rewarded blocks (W+: 196 ± 13 s, W-: 185 ± 4 s, t-value = 4.3, p-value = 2.0 x 10^{-4}). (**D**) Average spout contact time in response to auditory and whisker trials in W- and W+ showing slightly faster response in W+ compared to W- for both auditory and whisker trials (Auditory: W+: 370 ± 9 ms, W-: 400 ± 9 ms, t-value = -8.7, p-value = 1.8 x 10^{-10}, Whisker: W+: 392 ± 9 ms, W-: 418 ± 9 ms, t-value = -4, p-value = 6.0 x 10^{-4}). (**E**) Left: average lick probability in response to whisker trials centered on block transition when contextual backgrounds are replaced by constant white noise. Right: same center on first trials around transition. Showing absence of context modulated response to the whisker stimulus when context is not explicitly and continuously given to the mice. (**F**) Example traces for whisker angle, jaw angle and pupil area. Vertical lines represent trial onsets: auditory, blue; catch, grey; and whisker, orange. (**G**) Tracking of face posture (whisker angle, jaw opening and pupil area) during quiet window preceding whisker trials sorted by context (top row) or by trial outcome (bottom row). Pupil area was significantly modulated by context with larger values in W+ compared to W- (W+: 0.52 ± 0.13 mm^2, W-: 0.50 ± 0.12 mm^2, t-value = 3.7, p-value = 0.023). Whisker angle and jaw opening were modulated by trial outcome with larger values in the baseline preceding lick for jaw opening (Lick: 0.27 ± 0.05 mm, No-Lick-: 0.23 ± 0.04 mm, t-value = 4.6, p-value = 0.0035), and smaller values in the baseline preceding lick for whisker angle (Lick: 97.3 ± 13 °, No-Lick-: 98.6 ± 12 °, t-value = -4, p-value = 0.0103). (**H**) Same as G, but for movement features (jaw speed and whisker speed). Jaw speed was significantly higher in W+ compared to W- (W+: 3.0 ± 1.0 mm/s, W-: 2.5 ± 0.8 mm/s, t-value = 5.1, p-value = 0.0011) and before Lick compared to No-Lick (Lick: 2.8 ± 0.1 mm/s, No-Lick: 2.6 ± 0.7 mm/s, t-value = -3.7, p-value = 0.0254). (**I**) Example tree extracted from the gradient boosted tree model showing the impact of parameter values on model decision. Each node of the tree corresponds to a decision step at which a parameter value is used to follow one branch or the other. Positive values in the final leaf tend to deviate the model toward predicting a lick whereas negative

values tend to deviate it toward predicting no lick. (**J**) Correlation matrix between the features used to train the behavioral model showing that the model parameters are decorrelated. (**K**) SHAP values for one example trial showing the impact of the parameter value (in grey) on the model prediction for this given trial. Positive values (in red) tend to deviate the model toward predicting a lick whereas negative values (in blue) tend to deviate it toward predicting no lick. (**L**) Performance of the model in one session held out from the training set.

Figure 2 – figure supplement 1

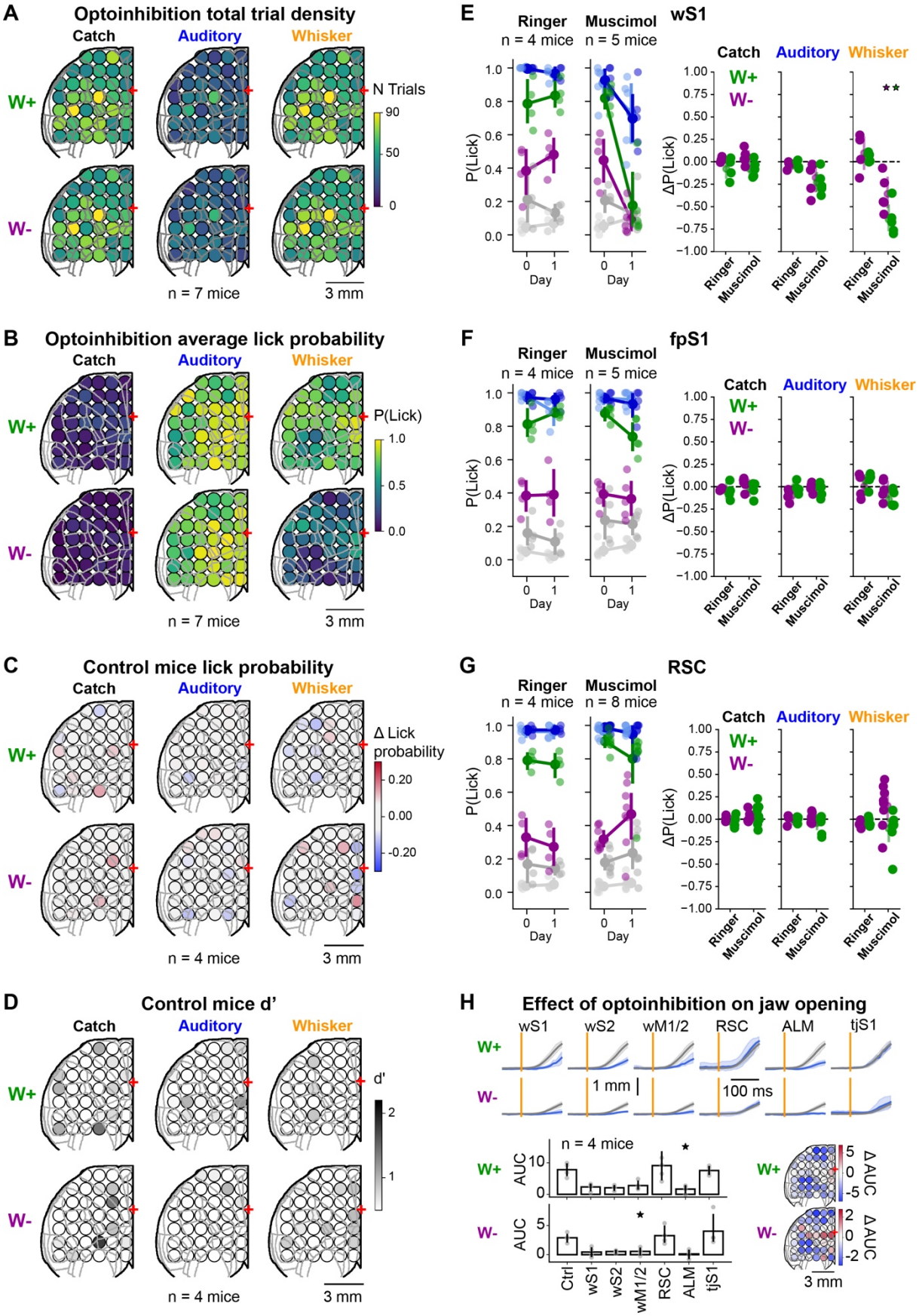

1379 **Figure 2 – figure supplement 1.** (**A**) Grid showing the total number repetitions of inhibition
1380 for each trial type and both contexts at each target location summed over the 7 mice. (**B**) Grid
1381 showing the absolute lick probability in catch, auditory and whisker trials in W- and W+. For
1382 each mouse we obtained a grid representation of the lick probability in response to each trial
1383 type in both contexts and further averaged these grids over mice. (**C**) Grid inhibition results in
1384 control mice not expressing ChR2. Grid map showing change in lick probability in response to
1385 catch, auditory and whisker trials in W- and W+ during optogenetic inactivation of the target
1386 area. Changes in lick probability are computed relative to lick probability in match trial type for
1387 each context in control stimulation trials, where the optogenetic laser beam is directed out of
1388 the brain. (**D**) Quantification of the optogenetic effect by computing d' between the distribution
1389 of ∆Lick probability in stim trials with a null distribution computed by shuffling all trials 1,000
1390 times. (**E**) Effect of wS1 muscimol or Ringer injection on task execution. Mice were trained until
1391 they reliably performed at expert level and on the test day, injections were performed just
1392 before the behavior session. Left: lick probability in response to catch, auditory and whisker
1393 trials in W- and W+ in baseline day 0 and in day 1 with either Ringer or muscimol injection.
1394 Right: change in lick probability in response to catch, auditory and whisker trials in W- and W+
1395 relative to the baseline day. Muscimol injection in wS1 significantly reduced lick probability in
1396 response to whisker trials in W- and W+ (hierarchical bootstrapping, p-value < 1.0×10^{-5}). (**F**)
1397 Same as in E, but for injection into the forepaw primary somatosensory cortex (fpS1), serving
1398 as an injection control. (**G**) Same as E, but for RSC inactivation, which leads to a non-
1399 significant positive trend in lick probability for whisker trials in W- (hierarchical bootstrapping,
1400 p-value = 0.059). (**H**) Top: traces of jaw opening aligned on whisker trials for control (grey) or
1401 inactivation of the target area (blue) in W+ and W-. Bottom: quantification of the area under
1402 the curve in the 150 ms following trial onset and grid representation of the average effect.

1403 # Figure 3 – figure supplement 1

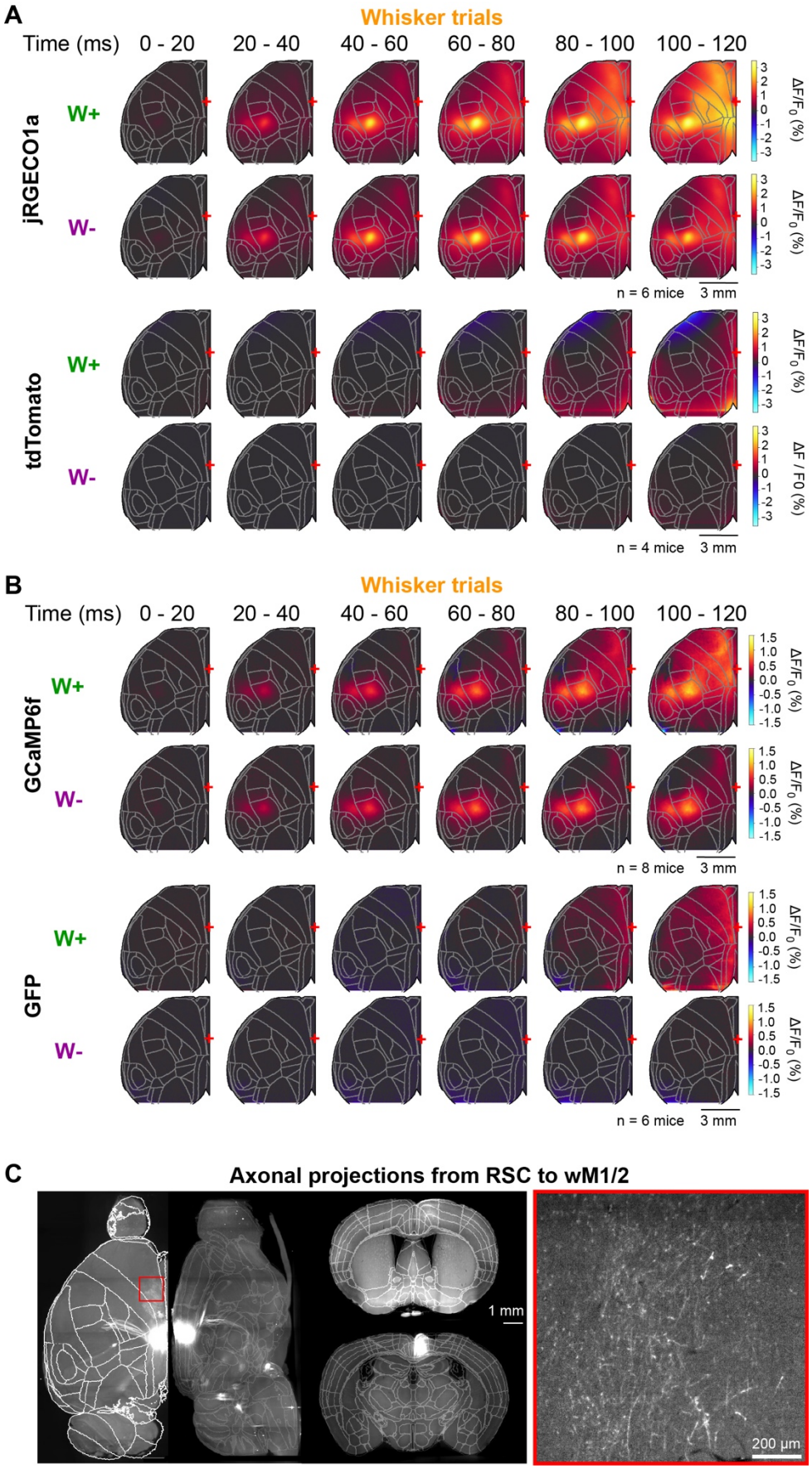

1404

1405 **Figure 3 – figure supplement 1.** (**A**) Image series showing evolution of cortical dynamics
1406 following whisker trials in W+ and W- in jRGECO1a (data duplicated from Figure 3F to facilitate
1407 direct comparison) and tdTomato control mice imaged under identical conditions. Early
1408 activation of primary and secondary whisker associated somatosensory cortices and
1409 propagation of sensory evoked activity were observed only in jRGCO1a expressing mice. (**B**)
1410 Same as A, but for GCaMP6f vs GFP mice. Sensory-evoked activity patterns in GCaMP6f-
1411 expressing mice were similar to jRGECO1a-expressing mice and not present in GFP-
1412 expressing control mice. (**C**) To image axonal projections from retrosplenial cortex, mice were
1413 injected with an AAV allowing for the expression of membrane bound opsin Chronos fused
1414 with GFP (AAV5.Syn.Chronos-GFP.WPRE.bGH). Injections were performed 1.5 mm posterior
1415 from bregma and 0.5 mm lateral at 4 depths from the pial surface (-200 µm, -400 µm, -600 µm
1416 and -800 µm, 25 nL / site). 4 weeks after injection, animals were perfused and brains extracted
1417 to be cleared and immunostained against GFP through iDISCO. We show light sheet imaging
1418 sections registered to Allen Mouse Brain Atlas after AAV injection in RSC in an example
1419 mouse. Left is a dorsal view of the cleared brain rotated 30 degrees to match the orientation
1420 in our widefield imaging. Middle panel is a sagittal view and coronal sections of the injection
1421 site (bottom) and M2 (top). Right panel shows branching axon innervating wM1/2 at higher
1422 resolution.

Figure 4 – figure supplement 1

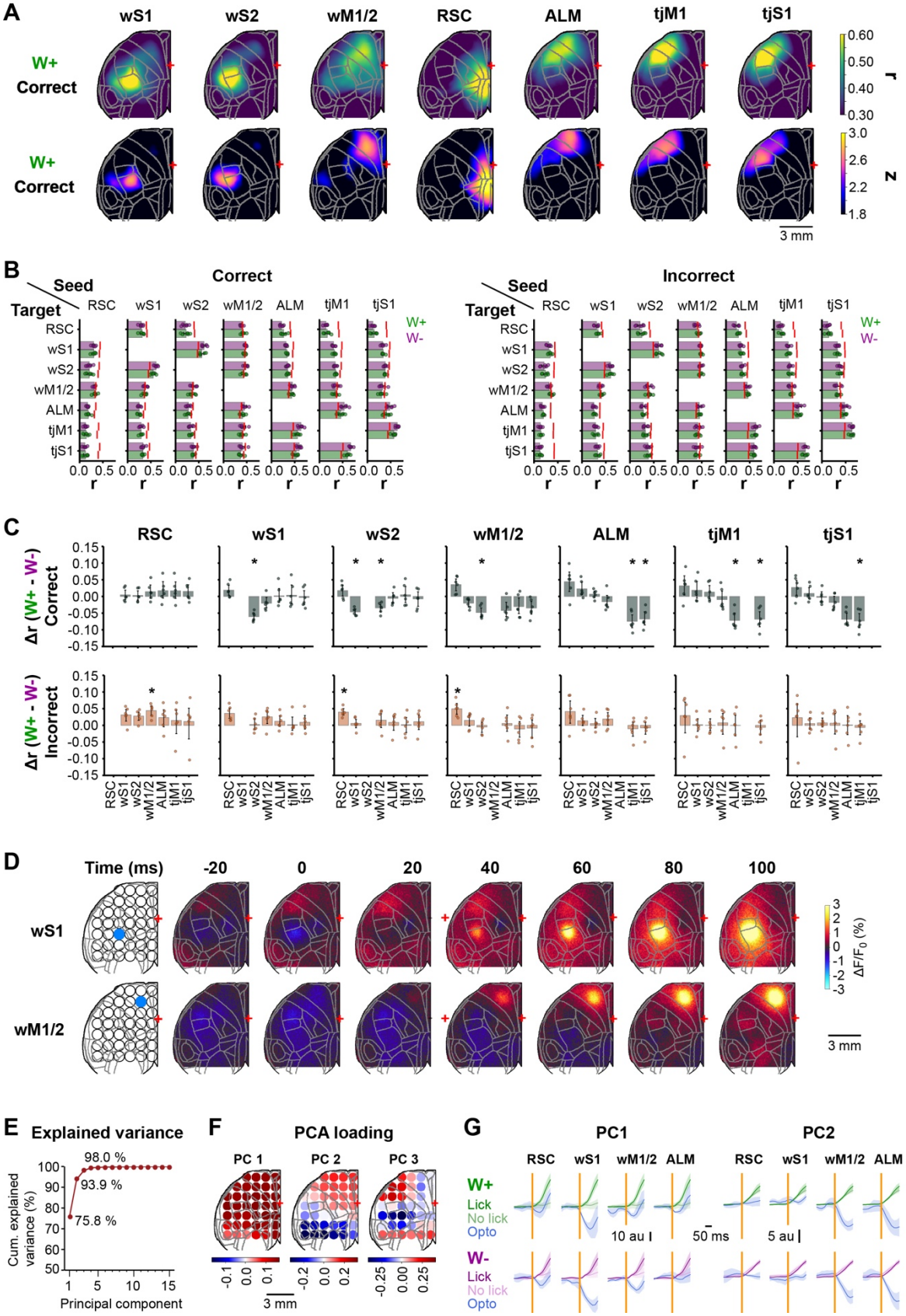

1426 **Figure 4 – figure supplement 1.** (**A**) Top row: correlation map for wS1, wS2, wM1/2, RSC,
1427 ALM, tjM1 and tjS1 seeds in correct whisker trials in W+. Bottom row: After data shuffling, we
1428 obtained for each seed and pixel a distribution of correlation value across shuffles. We
1429 represented for each seed a map showing the number of standard deviations of the correlation
1430 in the observed data compared to shuffled data. (**B**) To investigate correlations between areas,
1431 we reduced the correlation maps to grid space. We show as bar plots the correlation between
1432 seed and target areas in W- and W+ in correct (left) and incorrect (right) trials. The red dashed
1433 line indicates statistical threshold for correlation values defined as 1.8 standard deviation of
1434 the shuffle distribution above the shuffle mean. This allows us to identify significantly
1435 'connected' regions, such as wS1 and wS2 or ALM and tjM1 in W+ and W- for both correct
1436 and incorrect trials. We used this criterion to obtain the 4 graphs of Figure 4B showing
1437 correlation between 'connected' regions in W+ and W- for both correct and incorrect trials. (**C**)
1438 Correlation changes across contexts between selected seed and target area for correct (top
1439 row) and incorrect (bottom row) trials. Stars indicate significantly different correlations in W-
1440 compared to W+. We used the d' associated with the amplitude of the context modulation Δ
1441 (W+ - W-) or the outcome modulation Δ (Incorrect - Correct) of the correlation for previously
1442 identified 'connected' regions to build the delta summary graphs shown in Figure 4B. (**D**) Image
1443 series showing evolution of cortical dynamics following optogenetic stimulation trials in naïve
1444 mice expressing the calcium indicator jRGECO1a - but not the ChR2 opsin - with opto-inhibition
1445 laser directed to wS1 (top line) and wM1/2 (bottom line). This control experiment shows a
1446 locally restricted jRGECO1a photo-activation effect (jRGECO1a is based on mApple, which
1447 shows photoconversion upon blue light stimulation), but no widespread inhibition as observed
1448 in mice expressing the ChR2 opsin in inhibitory neurons (Figure 4C). (**E**) Cumulative variance
1449 explained by the first 15 components resulting from PCA analysis. (**F**) Grid representation of
1450 the loading on the first 3 PCs of each of the grid locations. (**G**) Time course of PC1 and PC2
1451 in W+ and W- for control and selected optogenetic inhibition points.